Theoretical studies of plasmon losses including elastic scatterings in Core-level Photoemisson spectra

January 2017

Noyuri YAMAMURA

Graduate School of Advanced Integration Science

CHIBA UNIVERSITY

(千葉大学学位申請論文)

内殻光電子分光における弾性散乱を含めたプラズモンロススペクトルの理論的研究

２０１７年　１月提出

（平成２８年度提出）

千葉大学大学院融合科学研究科
ナノサイエンス専攻
ナノ物性コース

山村　野百合

Contents

Abstract

Quantum Landau formula gives overall features in core-level photoemission spectroscopy, including plasmon satellite. The final purpose of our theoretical approach is to find out the electron density and geometry of substances through the behaviors of emitted photoelectrons from the solid, that can be observed in the nano structure on the quantum physics. We calculate here the plasmon loss spectrum with this formula and discuss the effect of the elastic scatterings. Li is a light element with elastic scattering effect and this effect is considered to be weak in the Li metal. We calculate the azimuthal scan of the 1st plasmon loss peak in an Al metal. This formula takes into account elastic scattering effect, so it enable us to calculate the azimuthal scan. We focus on the depth dependence of the azimuthal scan of the plasmon loss peak.

Chapter 1

General Introduction

Quantum Landau formula gives overall features in core-level photoemission spectroscopy, including plasmon satellite. Here we present the quantum Landau formula and show the calculation results of Al 2s photoemission and Li 1s photoemission. The final purpose of our theoretical approach is to find out the electron density and geometry of substances through the behaviors of emitted photoelectrons from the solid, that can be observed in the nano structure on the quantum physics.

In the end of the 19th century, Photoelectron spectroscopy (PES) was a modern experimental method based on the Photoelectric Effect [1]. Hertz detected the phenomenon of photoemission in 1887 [2]. In 1905, Einstein found the reason why the kinetic energy of the ejected photoelectron doesn't depend on the intensity of the incident light, but it depends only on their wavelength [3]. He succeeded illustrating what is the Photoelectric Effect by using his new idea about light, the quantum nature of light. The Einstein Photoelectric law $E_{kin}^{max} = \hbar\omega - \phi$ gives the energy relationship between a photon and an emitted photoelectron. The energy of the impacting atom, $\hbar\omega$, with the work function ϕ of the target, which is the minimum quantity of energy which is required to remove an electron to infinity from the surface of a given solid, and the kinetic energy, E_{kin}^{max}. Kai Siegbahn developed the method of Electron Spectroscopy for Chemical Analysis (ESCA) , X-ray photoelectron spectroscopy (XPS) [4]. X-ray photoelectron spectroscopy (XPS) is a widely utilized method for searching characters of the surface and bulk properties of various kinds of materials. We study plasmon features in XPS; typical core-level X-ray photoemission spectra in metals have plasmon satellite peaks with a main noticeable peak. Lars Hedin studied complex electric systems and contributed to make good progress in many ingenious spectroscopic theoretical equations, by linking theory with experiment [5, 6, 7, 8, 9, 10]. Takashi Fujikawa expanded his stud-

ies for electron spectroscopy and X-ray spectroscopy, which was related to electron-photon interaction [11, 10, 12, 13, 14].

Now we focus on how the quantum Landau formula was constructed. Plasmon is the collective oscillation of electrons that have profound relation to the optical potential. Optical potential is described as green function and screened Coulomb potential [5] which is described by bare Coulomb potential and the dielectric function. We have described the phenomena of a high number of electrons including plasmon by the screened Coulomb potential with the term of the dielectric function.

1.1 Dielectric Function and Plasmon

1.1.1 Dielectric function

In general dielectric function is defined as that for response of the materials to the external electric field [15]. In the classical physics, this function gives us $D = \epsilon E$ (ϵ for the response of solids and E is the external electric field) [16]. The dielectric function describes how the substance behaves when it is in the external electric field and it leads us the fundamental understandings of materials.

The dielectric function can be derived from the experimental data of the reflection of light. This function depends on the frequency of light, so it is written as $\epsilon(\omega)$. The dielectric function is defined as the square of the complex refraction index; $\sqrt{\epsilon(\omega)} \equiv n(\omega) + iK(\omega)$, where the real part $n(\omega)$ is the refractive index and the imaginary part $K(\omega)$ is the extinction coefficient [16]. The reflectivity coefficient $r(\omega)$ (complex value) described by $n(\omega)$ and $K(\omega)$. Expressing it in the polar form of complex number, its square of the absolute value $|r(\omega)|^2$ is regarded as the reflectance $R(\omega)$ as the phase of the reflected wave $\theta(\omega)$. We can experimentally observe the value of reflectance R from the light reflection. These relations enable us to give the value of the dielectric function by measuring the reflectance R and phase $\theta(\omega)$. The value of the phase of reflected waves $\theta(\omega)$ is hardly obtainable in the experiments, but it is possible to obtain it by using Kramers-Kronig relation with the value of the experimentally measured reflectance R, in the case of linear response of solid [16]. It means that the solid gives an output which is a linear combination of input; for the dielectric function, the electric flax density D can be written as a linear term of the external electric field. Figure (1.1) shows the Aluminum reflectance, and Figure (1.2) shows the dielectric function derived from the reflectance [18].

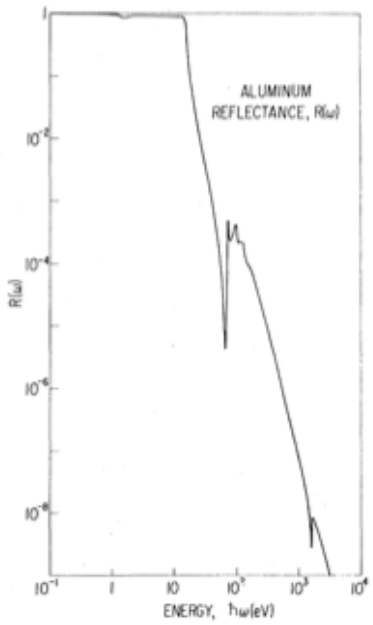

Figure 1.1: Reflectance of metallic aluminum at room temperature [18]. Reprinted with permission.

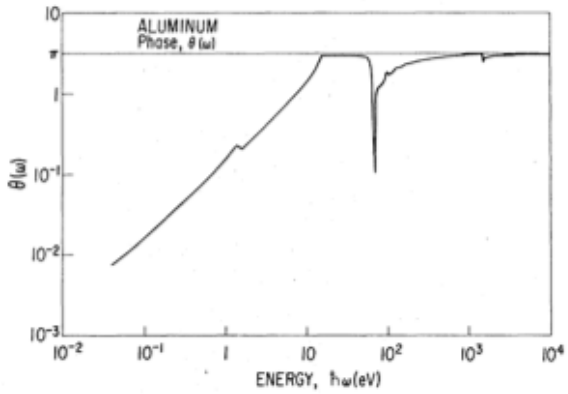

Figure 1.2: The phase $\theta(\omega)$ of the reflectivity of metallic aluminum at room temperature as calculated from the reflectance values of Figure 1.1 via Kramers-Kronig analysis [18]. Reprinted with permission.

Another method for acquiring the dielectric function in experiment is Electron Energy Loss Spectroscopy (abbreviated as "EELS"). EELS measures the energy losses ΔE of injected electrons which transmit a thin film of the solid or reflect at the boundary of the solid [23]. The experimental result for EELS is described with the imaginary part of inverse of the dielectric function $Im(-1/\epsilon(\omega))$, that is the loss function. Kramers-Kronig relation, gives its real part $Re(1/\epsilon(\omega))$. Then we get a dielectric function from EELS experiment. Mkhoyan *et al.* showed the analysis of dielectric function of Si [29], see Figure (1.4) and Figure (1.5).

1.1.2 Plasmon

Plasmon is a quantized plasma oscillation, a collective motion of electrons in a plasma [24]. Plasma oscillation is a compressional wave of electronic charges, in which the electron density has a periodic pattern as a longitudinal wave. There are two patterns for an oscillation of electrons; the longitudinal oscillation which produces the fluctuation of electric density, and the transverse oscillation which doesn't change the electric density in a free electron gas. A large number of electrons in a solid behaves collectively. Plasmon behaves differently from an electron in an atom. Plasmon can be excited as a response for external electric field and it can be described by the dielectric function as we have mentioned.

In general, there are two types of plasmon loss, and both of them have their eigen-frequency which can be determined by the dielectric function. Bulk plasmon is the oscillation of the electric density around the slab with the electric density n [23]. In the case of bulk plasmon, electrons oscillate in the same direction as the plasmon wave propagation. In other words, the electric field with the longitudinal oscillation is parallel to the plasmon wave vector q. In this case, the magnetic field H by the convection current from oscillating electrons and that by displacement current from plasmon wave compensate each other, therefore $rotH = 0$, there is no magnetic field in the solid [23]. With Maxwell equation, we can illustrate the condition for the eigen-frequency as $\epsilon(\omega) = 0$. This eigen-frequency ω is given as complex value because the value of the dielectric function is complex. The imaginary part of ω pictures of the damping of plasmon wave. The value of eigen-frequency ω is determined by the dielectric function. We take the relaxation time as the time that the plasmon waves vanish by gradual damping. When the plasmon becomes stable, its relaxation time should be treated as infinite. The eigen-frequency in this condition becomes the bulk plasma frequency $\omega = \omega_p$ which depends on the electric density n.

When the energy of the external electric field is above $\hbar\omega_p$, bulk plasmon is excited. Surface plasmon

is a collective excitation which occurs at the boundary between two different materials [23]. Longitudinal waves of the surface charge density run along the surface as a polarization wave. The displaced charges produce an electric field with components parallel and components perpendicular to the boundary. In contrast to the case of balk plasmon, the magnetic field has components H_x or H_y in the plane surface. This field configuration propagates with the phase velocity ω/k_x. The eigen-frequency ω of these waves is connected with by a dispersion relation deduced from Maxwell equation. For the semi-infinite jellium model (free electron gas model), we can get the eigen-frequency $\omega = \frac{\omega_p}{\sqrt{1+\epsilon_0}} \equiv \omega_s$ from the dispersion relation (See [23]). If we took ω_s as 1 (vacuum in a.u. unit), it becomes $\omega_s = \frac{\omega_p}{\sqrt{2}}$.

The electric function depends on not only frequency ω but also wave vector q. We obtain the dielectric function $\epsilon(\omega, q = 0)$ at $q = 0$ and that is the dielectric function derived from the experimental reflectance of the light and the dielectric function of the free electron gas. Lindhard gave the formula of the dielectric function $\epsilon(\omega, q)$ of Fremi gas with the wave vector q dependence in the first time. The external perturbation in this free electron gas model leads to the interband transition. In this model we can describe the response to the external field as the momentum transfer $\hbar q$ with the interband transition. Using Lindhard dielectric function at the relaxation time $\tau = \infty$, we can obtain the eigen-frequency $\omega(q)$ by the condition for the longitudinal oscillation $rotH = 0$ at $q << q_F$ (q_F is fermi wave number). That is called the theoretical dispersion relation of bulk plasmon.

The dielectric function is a response function and it has a frequency as a variable, corresponding to the energy loss which changes according to the external electric field. We describe the dielectric function $\epsilon(\omega, q)$ when it response to the electron which lost energy $\hbar\omega$ and momentum $\hbar q$.

1.2 Plasmon Features in Experiment

The characteristic of plasmon loss correlate the polarizability of the material, which relate to the dielectric function [23]. We observe a solid through plasmon in two ways; in one way we inject the light (the electromagnetic wave) into the solid, and in the other way we inject electrons into the solid.

1.2.1 Light Absorption

In the first way, the reflection of the light occurs as the phenomenon connecting deeply with the plasmon, and the bulk plasmon (the longitudinal oscillation) is produced by the gradient of electron density which is originated in the interaction between the light and charges in surface. That is, the light resonants and is absorbed in the collective electrons at the light frequency $\omega > \omega_p$. This absorption is rather weak, but distinctively observed in the thin metal film. Therefore, the dispersion relation for the light absorption is obtained with the dispersion relation of the bulk plasmon in free electron gas which we mentioned and the resonance condition $\omega > \omega_p$. We show the transmittance of Ag films of different thickness, and we can see the resonances for volume plasmon frequencies.

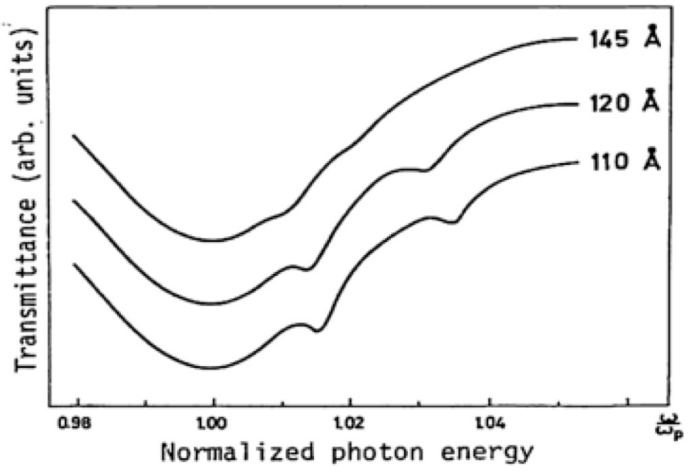

Figure 1.3: The transmittance of Ag films of different thickness for p polarized light [25]. The angle of incidence is 75°. There is resonances for volume plasmon frequencies at the wave vectors $q = \frac{n\pi}{D}$ with n = 3 and 5. Reprinted with permission.

1.2.2 Electron Energy Loss Spectroscopy

In the second way, we study the interaction between the electron current and plasmon, for example EELS and XPS. The electron injected into the solid and inelastically scattered in the solid, and the X-ray photoemission spectroscopy (XPS) detect photoelectron with the photoexcitation by injected X-ray. Both of them are affected by the inelastic scattering between electron and plasmon, and they depend on the loss function, contacted deeply connected to the dielectric function. The excitation of plasmon is firstly observed in EELS spectra, in which the probe electrons suffered energy loss and scattered inelastically during the transmission of thin film [26, 27]. The position, half-width and the intensity of energy loss peak (containing plasmon loss) observed by EELS correlate with the polarizability which is written by dielectric function $\epsilon(\omega, q)$ (the polarized electric field is created repulsively against electrons' propagation). So, Energy loss intensity of EELS is described in the form of the loss function, the imaginary part of the inverse of the dielectric function. In EELS, we measure how much electron energy is lost (ΔE) and what angle of the injected electron from the initial direction is diverged ($\vec{\theta}$). The momentum transfer $\hbar q$ by the inelastic scattering have calculated using the value ΔE and $\vec{\theta}$ so we can obtain the value of momentum q from the experimental result.

The EELS have two methods; the reflection method and the transmission method. The former is the method to observe the reflected electrons so it is sensitive to the surface and we can observe strong peaks of surface plasmon. Observed multi-plasmon loss structure represents that reflected electrons suffer multi-inelastic-collision or multi-energy-loss in once collision. The later is the method to observe transmitted electrons through a thin film. Its intensity depends on the film thickness which should be thinner than the mean free path of the injected electron (the mean free path is the average distance, how long electrons can run in a solid interval of inelastic scatterings). Figure (1.5) shows the spectra with the transmission method in Si film. We can see that it depends on the thickness of the film, and the multi-plasmon loss peaks become larger as the film becomes thick. The weak 1st surface plasmon peak is observed in Figure (1.5), which is much smaller than that in Figure (1.4). The surface plasmon peaks are higher as usual in the reflection EELS according to the surface sensitivity, whereas the bulk plasmon peaks are too high to compare with the surface plasmon peak in transmission EELS because probe electrons pass through the solid in long distance.

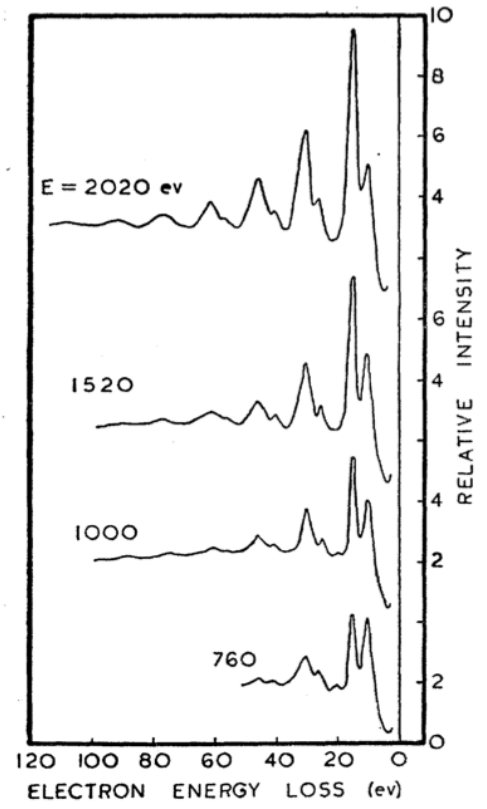

Figure 1.4: The refection EELS in Al thin film with injected electron energy 760 eV, 1000 eV, 1520 eV, 2020 eV by C. J. Powell and J. B. Swan [28]. It has bulk plasmon peak at 15.3 eV and the surface plasmon 10.3 eV in 1st loss peak. Multiple loss peaks are observed. Reprinted with permission.

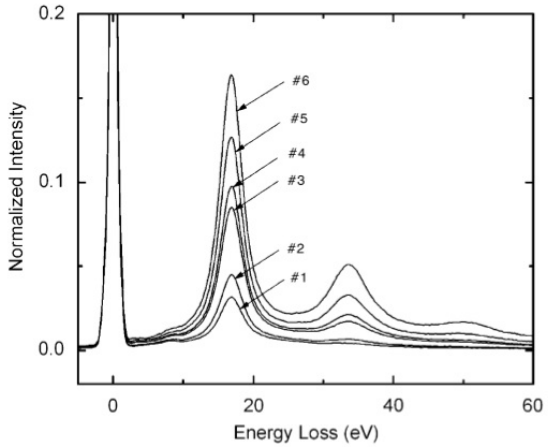

Figure 1.5: The real and imaginary parts of the dielectric function of Si deduced from single bulk plasmon peak [29]. The curves labelled 'corrected' correspond to results when surface-losses were removed. The specimen thickness is 420 Å. Reprinted with permission.

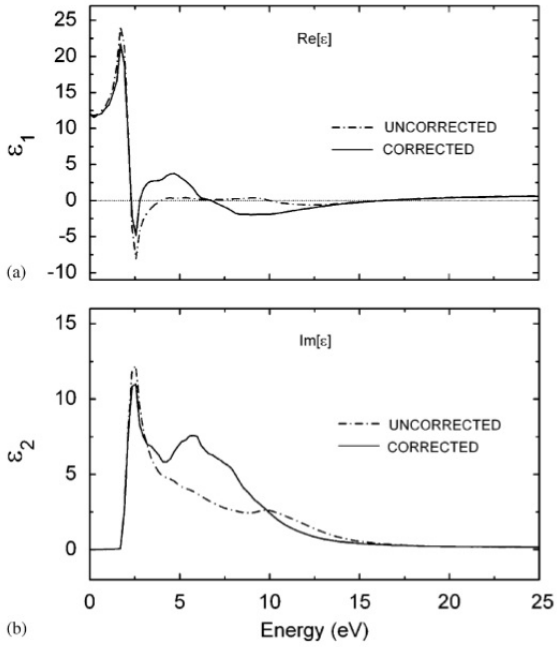

Figure 1.6: The real and imaginary parts of the dielectric function of Si deduced from single bulk plasmon peak [29]. The curves labelled 'corrected' correspond to results when surface-losses were removed. The specimen thickness is 420 Å. Reprinted with permission.

1.2.3 X-ray Photoelectron Spectroscopy (XPS)

XPS is a method of experiment to detect photoelectrons, and it is a powerful method to know the microscopic information of material. In XPS, we excite the state of solid by injected X-ray and detect the photoelectron emitted by photoexcitation of solid. Since Koopmans found that the ionization energy of the solid corresponds to the orbital energy which shows how strongly the core electron bounded, Siegbehn developed the XPS method in order to figure out the core orbital state. In XPS, we obtain the peak at the point of the binding energy correspond to the core orbital energy. The value of binding energy E_b is $E_b = h\nu - E_k - \phi$ ($h\nu$ is the photon energy of injected X-ray, ϵ_k is the kinetic energy of detected photoelectron and ϕ is the work function). When we compare the position of a material and that of single substance in the same core-level, we obtain the chemical bonding state from the chemical shift.

Because XPS is a surface sensitive method, whose sensitivity depends on how short the photoelectron's mean free path. To utilize the sensitivity to the surface, we can operate the depth composition analysis by changing the angles of detection. The refraction method in EELS also has sensitivity. Both of them use electrons as a probe, which use different phenomena; XPS, the photoelectric effect, and EELS, the inelastic scattering. They have the similar shapes of the spectra in metals and semiconductors. XPS gives unique spectra affected by the inelastic scatterings in metals and in semiconductors. They shows zeroloss peak (Doniach-Sunjic or Mahan lineshape), bulk plasmon peaks, surface plasmon peaks, and background [30]. Especially, the asymmetry shape of zero loss peak and the plasmon satellite (bulk plasmon peaks and surface plasmon peaks) are unique in metals and semiconductors (nearly free electron systems). The reason for the zero loss peak / asymmetry is that the electron-hole pair excitation affects to only one side of the peak, in the condition that it occurs when there are electrons in conduction band in the solid with core-hole potential by photoexcitation [30]. The plasmon loss satellite occurs because photoelectron loses their energy by the shake-up effect with core-hole potential (intrinsic plasmon) and by inelastic scattering from electrons (extrinsic plasmon). Because this inelastic scattering makes the solid electrons oscillate collectively (that phenomenon is plasmon), the photoelectrons lose the energy with the eigen-frequency of plasma. As it gives discrete (quantized) energy loss, a satellite structure appears in XPS. On the other hand, the electrons also suffer continuous (unquantized) energy loss by electron-electron and electron-ion collision and this effect makes featureless and smooth background in XPS spectra [30]. When we analyze XPS, we detect XPS background from XPS spectrum and we make

the experimental peaks fit with no loss peak and plasmon loss peaks. Figure (1.6) shows the wide range of Al 2s core-level XPS spectrum in Al single crystal, and zero loss peak and plasmon loss peaks are given by peak fitting [31]. Both of the no loss peak and plasmon peaks have asymmetry shapes, with longer tail in the high binding energy side (high loss energy side). The surface plasmon loss peaks appear at the side of the large bulk plasmon peaks. Plasmon loss structure in XPS has multi-plasmon loss peaks, as well as that of the reflection EELS. The former has asymmetric form of plasmon loss peaks, but the latter has symmetric form of those.

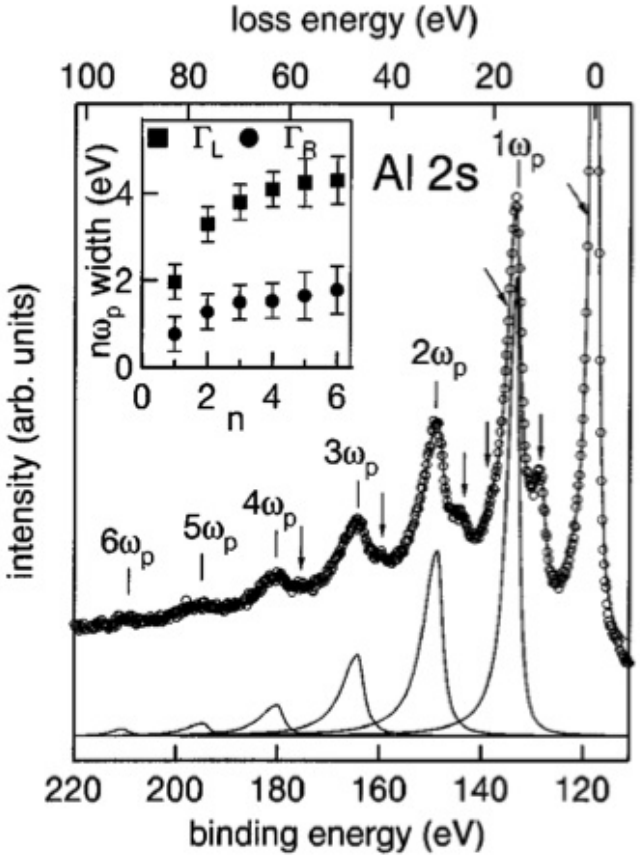

Figure 1.7: Wide range Al 2s core-level spectrum recorded at $\theta = 45°$ (experiment: open circles; fit: solid line through experimental data) showing multiple (n=1-6) bulk plasmon excitations ($n\omega_p$) [31]. Vertical arrows indicate the energy positions of the multiple bulk and surface plasmon excitations related to Al 2s. The deconvoluted $n = p$ line shapes (solid lines) are shown at the bottom. Reprinted with permission.

1.2.4 X-ray Photoelectron Diffraction (XPD)

X-ray Photoelectron Diffraction (XPD) is the method of measuring XPS whose purpose is to find out the scattering features of electron intensity of the final-state [32]. XPD is a established technique that can research surface structure [33]. XPS is the experiment to measure the photoelectron current in the condition that specimen is fixed as a function of the photon energy, or as a function the binding energy, and X-ray Photoelectron Diffraction (XPD) is the experiment to measure the photoelectron current in the different polar and azimuthal angles [34]. The photoexcited electron is scattered and it pass through the crystal on its way to the surface, by the crystal potential [30]. A number of photoelectron waves occur in the elastic scattering of the primary photoelectron beam from the other ions in the crystal. The interference between elastically scattered waves can make its interference patterns. The interference pattern is to be measured by varying the azimuthal or polar detection angle of the photoelectrons.

XPS and XPD involve a process that can be linked to a LEED process, and the final state wave function of XPS and XPD correspond to the LEED-type wave function. Multiple scattering, scattering effect that a photoelectron experience several scattering events, should be taken into account when we model all elastic scattering effects [32].

Analysing XPD patterns of plasmon-loss peaks accompanying core lines enable us to distinguish from how much depth below the surface the emitters contributing to the total intensity come [34]. Experimental photoemission intensity is observed by the sum over lattice sites of photoelectrons. Each electron-atom scattering events with the diffraction patterns observed in the experiment have sharp peaks into the forward direction at energies higher than around 200 eV. XPD experiments are performed by scanning the azimuthal and polar angles under which the electrons are detected, but cannot be performed by scanning the depth of photoelectrons. Therefore, a depth profile of photoemission intensity is obtained from a calculation based on scattering theory. It has been suggested on the basis of multiple scattering calculations [35, 36] that if more than one scattering atom is placed along the emission direction, these forward-scattering effects are noticeably reduced according to a dephasing of the electron wave after the photoelectron passed the atoms nearest to the emitter. There would be more chances that photoelectrons pass through atoms if it is emitted from the deeper layer. The defocusing effect depends on the depth of photoelectron emission. Defocusing length is estimated from the experimental XPD patterns of plasmon-loss peaks accompanying core lines. Figure (1.8) shows azimuthal scan at $\theta = 45°$ for the Al

2s core line, the first, the second, and the third plasmon-loss peak accompanying this line from Al(001) single crystal.

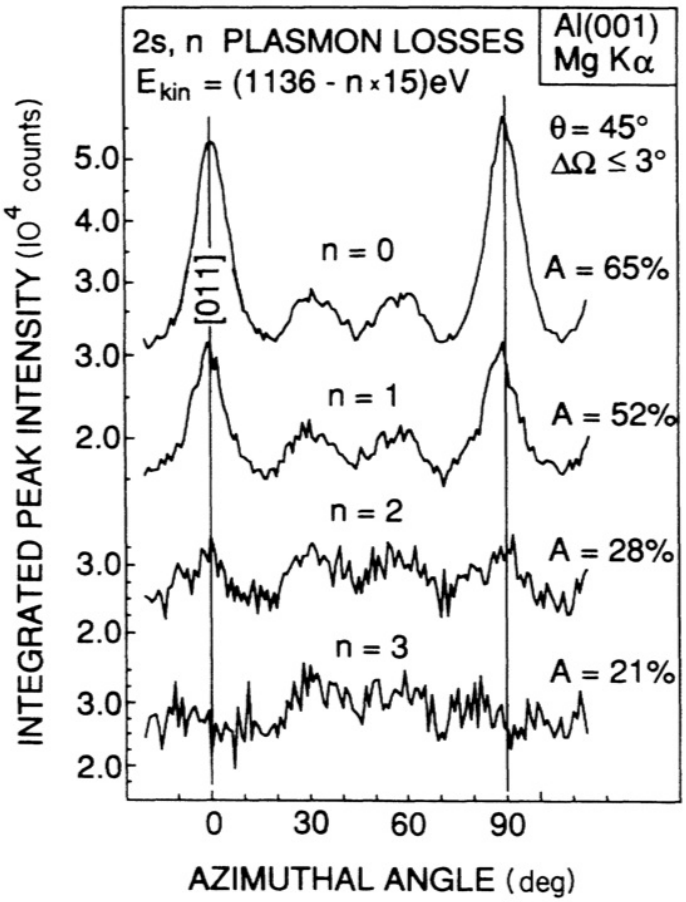

Figure 1.8: Azimuthal XPD curves from a (001) single crystal of Al, measured with Mg Ka radiation, for the 2s core level (E_B =118 eV) and the first three (n=1,2, and 3) associated plasmon-loss peaks ($\hbar\omega_p$ =15 eV) [34]. The polar angle was $\theta = 45°$. The scans in the azimuthal direction covered a range of 120°, including two (011) directions (main maxima for the no-loss line). Reprinted with permission.

1.3 3 Theoretical Studies of Plasmon Structure in XPS

1.3.1 Discussion of Plasmon loss Studies

Photoemission can be thought of as a three-step process consisting of [37];

(1). photoexcitation of the photoelectrons,

(2). the travel of the photoelectrons through the crystal,

(3). the escape of the electrons over the surface barrier (electron affinity) into the vacuum.

The energy loss for a photoelectron by plasmon excitations (we call this phenomena "plasmon loss") occurs in the case (1) and (2). In the case (1), the sudden potential change caused by the formation of a core hole attracts the conduction electrons to screen the core-hole and leads to the intrinsic plasmon excitation. In the case (2), the extrinsic plasmon is excited by the Coulomb interaction of the conduction electrons with the photoelectron passing through the solid from the photoemission site to the surface.

There are two approaches for treating plasmon peak intensities in photoemission;

a. three step model (Berglund-Spicer (BS) model in ref [9]) In three step model, that intensity is given by a convolution of the spectral function corresponding to intrinsic plasmon excitation process with a loss function corresponding to entrinsic plasmon excitation process,

b. one step model (the quantum-mechanical (QM) model in ref [9]) In one step model, that intensity is given by the square of the total amplitude, which is the sum of intrinsic and extrinsic plasmon amplitudes.

Berglund and Spicer (1964) presented three step model, and discussed the extrinsic plasmon losses [37]. The three step model is expressed by a convolution of the spectral function $A(\omega)$ with a loss function [9]. This model is useful for practical purposes [38, 39, 40, 41].

On the other hand, Inglesfield (1981) demonstrated the calculation of single plasmon peak in one step model, in which the process of photoemission is studied in the Golden rule formulation using perturbation theory [52, 42]. One step model includes quantum-mechanical interference between intrinsic plasmon loss and extrinsic plasmon loss [42, 7, 9]. Inglesfield (1983) found that interference between intrinsic and extrinsic excitation reduces the long-wavelength surface and bulk plasmon excitation [42],

and the plasmon peaks disappear in low photoelectron kinetic energy, this phenomenon was observed in experiment [43, 44, 42]. Uwatoko *et al.* (2001) showed that the one step calculation explains well the experimental features [45].

Hedin *et al.* (1998) showed the process of the transition from one step model to three step model, and he discussed about three models [9]:

- Quantum Mechanical (QM) model derived from one step model
- Semi Classical (SC) model, where the photoelectron is put on a trajectory and not allowed to recoil,
- Berglund and Spicer (BS) model derived from three step model.

The interference in QM model caused a strong suppression of the satellite structures as compared to that in the BS model at low kinetic energy [9]. The SC approach agrees with the quantum mechanical one at high energies [46]. Shinotsuka *et al.* (2008) performed QM calculation put forward by Hedin taking the interference effect into account [47]. Interference plays a destructive role especially at the low energy ($\hbar\omega$ = 125 eV), whereas extrinsic contribution is dominant at the high energy ($\hbar\omega$ = 1486.6 eV).

1.3.2 Many Body Theory for plasmon loss

Methods to calculate the plasmon loss peaks in photoemission spectra including both elastic and inelastic scattering have been studied. Fujikawa and Hedin (1989) studied the scattering theory which is valid for elastic and inelastic scattering [10]. Their results are written in terms of one-electron expressions involving damped one-electron functions and optical potentials. Fujikawa developed the method of this scattering theory for deep core excitation EELS [48], EELS [12], XPD [47], and XPS with plasmon loss peaks [14].

We have studied theoretical approach on plasmon loss peaks in XPS based on quantum mechanics, using multiple scattering theory. In XPS, the injected X-ray makes a core electron in the bound state excite, and the core electron becomes a photoelectron in the continuum state. The multiple scattering theory is available for the calculation for the amplitude of XPS. The amplitude of XPS in multiple scattering theory describes every states, from the initial state to the final state including scatterings in their interval. T matrix describes that amplitude and phase of the photoelectron change according to the scattering of electron by an atom, and the green function describes the propagation of electron. One

product of green function and t matrix corresponds to one scattering event. The calculation of the XPS amplitude requires the initial state and the final state, evaluating how much amplitude and phase of the photoelectron changed by the scattering in an atom, we can calculate the amplitude in XPS. Multiple scattering theory doesn't require that the initial state and the final state have same bases. Consequently, multiple scattering theory is appropriate with the calculation for the amplitude of XPS that has different the bases for the initial state (the bound state) from that for the final state (the continuum state).

XPS formula (1985) derived by Bardyszewki and Hedin which can explain how single plasmon peak relates to the optical potential and the fluctuation potential [7]. The fluctuation potential represents a induced potential by the displacement of the electric density. We can associate this potential with plasmon because plasmon is the longitudinal wave, the density oscillation. The optical potential is complex and non-local potential. The photoelecric effect observed in XPS makes a electron transit in the one state to in an another, therefore it can be written by Fermi's golden rule [6]. In this model, the operator of the electric magnetic field $\sum_i [-\frac{e}{mc}\boldsymbol{p}_i \cdot \boldsymbol{A}^2(\boldsymbol{r}_i)]$ excites the core electron and makes it a photoelectron. That model treats one electron formula, but we have to treat electrons which behave together in a solid. Goldberger and Watson (1964), were taken the basement on their study on the many body model, and presented the formula for photoelectron intensity with certain solid angle Ω and certain energy ϵ_f [49]. This formula based on Fermi's golden rule, and takes the initial state as the ground state of the solid (the state before the excitation) and the final state as the excited state of the solid which lost one electron. The final state depends on the quasi-particles (for example photon, plasmon and etc.). Bardyszewki and Hedin (1985) studied on plasmon excitation and constructed the theory which describe the plasmon loss peak in XPS in metals [7]. They introduced the formula of Goldbarger and Watson to the photocurrent amplitude in XPS to expand scattering theory. They expressed the final state with Lippman-Schwinger equation with the green function. They describes the final state with the perturbation. They adapted the perturbation term in Hamiltonian as the fluctuation potential which Inglesfield (1981, 1983) took into account when he calculated extrinsic plasmon loss [52, 42]. The amplitude can be calculated independently in each two parts; intrinsic part and extrinsic part with VG. He explained intrinsic term by the fluctuation potential limited by core orbital. Langreth (1971) and Lundqvist (1969) calculated multi-plasmon loss satellite in XPS only focusing on intrinsic term (ignoring extrinsic term) [50, 51]. As a result, Hedin succeeded to find the dynamical structure factor $S(\omega)$ gives the intrinsic plasmon loss intensity. The dynamical structure $S(\omega)$ depend on the dielecric function (this is related with EELS). In addition, the amplitude in

XPS has the full green function with perturbation V, so we should expand it with the projection method which divide the part of a certain excitation state from the other parts. This expansion allows us to put the damping effect in the optical potential in the plain wave for the photoelectron, instead of non-damping plain wave (that is common use of this equation). The damping of the plain wave can be regarded as the decrease of the detectable photoelectrons affected by the optical potential. In this expansion, plasmon loss spectrum in XPS is affected by the fluctuation potential, and the photoelectrons in XPS decreased by the optical potential.

We have taken the calculation with the term of elastic scattering in XPS, following the Hedin's method. The excited optical potential determines the propagation G (the green function). Fujikawa and Hedin (1989) succeeded to describe the optical potential in the excited state as that in the ground state shifting its energy [11]. Fujikawa and Arai (2002) demonstrated, the formula for multiple plasmon loss in the form of Keldysh [13]. Shinotsuka took into account the effect of elastic scattering at the 0th plasmon loss XPS intensity (the 0 loss peak) and showed the depth distribution function [47].

Meanwhile, we have also explored the formula without the fluctuation potential. Hedin *et al.* (1998) found the calculation formula counting multiple plasmon losses with the intrinsic and extrinsic plasmon without the elastic scattering effect [9]. He associated the fluctuation potential with the screened Coulomb potential. Fujikawa (2008) carried on this idea and described the multiple plasmon loss with the elastic scatterings using approximation which was made under the assumption that the momentum of the photoelectron does not change in inelastic scattering [14]. In this exploration, we treat the fluctuation potential as the screened Coulomb potential. The screened Coulomb potential depends on the dielectric function. Kazama (2014) calculated the 1st plasmon loss with this formula [53].

We calculate here the plasmon loss spectrum with this formula and discuss the effect of the elastic scatterings. Li is a light element with elastic scattering effect and this effect is considered to be weak in the Li metal. We calculate the azimuthal scan of the 1st plasmon loss peak in an Al metal. This formula takes into account elastic scattering effect, so it enable us to calculate the azimuthal scan. We focus on the depth dependence of the azimuthal scan of the plasmon loss peak.

Chapter 2

Theory of Photoemission in Nearly Free Electron Systems

Typical core-level X-ray photoemission spectra in nearly free electron systems (i.e. Metal and Semiconductor) have plasmon loss bands in addition to a main sharp band. In this chapter we try to present definitions and basic concepts of theory of photoemission. This chapter provides two calculation formulas derived by Fujikawa; the quantum one-step formula based on many-body theory (section 2.1) and the quantum Landau formula (section 2.2) [14].

To make the discussion more firm we start with some simple basic definitions and elementary derivations. For zero temperature the initial state is the ground state of the system, $|\Psi_0\rangle$. The final state has a photoelectron "k", and the state of the remaining electrons is defined as "m". We need to know the final state also when the photoelectron is inside the solid, and we use the notation $|\Psi^-_{n\boldsymbol{k}}\rangle$ for a wavefunction where the photoelectron motion is correlated with that of the other electrons.

2.1 Many-body Scattering Theory

Many-body scattering theory is widely used for Electron Spectroscopy. To study XPS, it is necessary to develop a reliable theory to correctly describe the inelastic scattering of the photoelectron. The general theory of electron scattering from solids has been developed by Fujikawa and Hedin [10]. It describes important many-body effects and it enable us to derive useful expressions for inelastic scattering. Here we apply this electron scattering theory to the core-level photoelectron spectroscopy; in particular

we study the 0th plasmon loss peak (main peak) and the 1st loss peak features in detail.

2.1.1 Photoemission Theory

Independent Particle Approximation

Here, we show the photoemission formula in the independent particle approximation. The photocurrent per unit solid angle and unit energy is given by [6]

$$\frac{\partial^2 \boldsymbol{J}}{\partial\Omega\partial\epsilon} \sim \sqrt{\epsilon_f} \sum_i^{occ} |\langle\phi_f|\Delta|\phi_i\rangle|^2 \delta(\epsilon_f - \epsilon_i - \hbar\omega). \tag{2.1}$$

$\hbar\omega$ is the energy of the exciting photon and Δ is the electron-phonon interaction. ϵ_i and ϵ_f are the energies of the electron in its initial and final states. The initial state wave function ϕ_i describes a bound electron and the function ϕ_f is the outgoing wave solution of the Schrödinger equation. It is the sum of a outgoing plane wave and incoming spherical waves and is characterized by the asymptotic behavior

$$\phi_f(\boldsymbol{r}) \sim \mathrm{e}^{i\mathrm{k}_f\cdot\mathrm{r}} + f(\hat{\mathrm{k}_\mathrm{f}})\frac{\mathrm{e}^{-ik_f r}}{r}. \tag{2.2}$$

This is not the wavefunction of the photoelectron. The asymptotic form of the photoelectron wave function is

$$\phi_f(\boldsymbol{r}) \sim \left(\frac{\mathrm{e}^{ik_f r}}{r}\right)\langle\phi_f|\Delta|\phi_i\rangle\,. \tag{2.3}$$

The vector $\boldsymbol{r}$ is the vector from the region of excitation to the position of photoelectron. Equation (2.3) can be applied when the region where $\Delta\phi_i \neq 0$ is sufficiently small compared to r. It follows that the detector should be set on far from the emitter of photoelectron.

Many-Body Theory

When we go beyond the one-electron model, the photocurrent can be obtained from many-body scattering theory [49],

$$\frac{\partial^2 \boldsymbol{J}}{\partial\Omega\partial\epsilon} \sim \mathrm{I}_{\boldsymbol{k}} = 2\pi \sum_n |T(n^*\boldsymbol{k}, 0)|^2 \delta(E_0 + \omega - E_n^* - \epsilon_{\boldsymbol{k}}) \tag{2.4}$$

with the transition matrix

$$T(n^*\boldsymbol{k}, 0) = \langle \Psi^-_{n\boldsymbol{k}} | \, \Delta \, | \Psi_0 \rangle \, . \tag{2.5}$$

$\epsilon_{\boldsymbol{k}}$ is the energy of the photoelectron, $\boldsymbol{k}^2/2$. E_0 and E_0 is the grand state energy of the solid without core hole and E^*_n is the grand state energy of the solid with core hole. ω is the photon energy of the incident X-ray. The total energy E is given by

$$E = E_0 + \omega = E^*_n + \epsilon_{\boldsymbol{k}}. \tag{2.6}$$

The $T(n^*\boldsymbol{k}, 0)$ is the scattering amplitude for the photocurrent. Ψ_0 is the ground state with (N) electrons and $\Psi^-_{n\boldsymbol{k}}$ is the final state with a photoelectron and (N-1) electrons in the target. $\boldsymbol{k}$ denotes one electron states of the photoelectron and n stands for the excitation state of electrons in the target.

This study bases on blue electron theory. We distinguish the photoelectron from electrons in the solid, therefore exchange effects between a photoelectron and the electrons in the solid are neglected. We follow an approach developed by Fujikawa and Hedin [10, 48],

$$H = H_s + T_e + V_{es}, \tag{2.7}$$

with

$$V_{es} = \sum_i \frac{1}{|\boldsymbol{r} - \boldsymbol{r}_i|} - \sum_\alpha \frac{Z_\alpha}{|\boldsymbol{r} - R_\alpha|}. \tag{2.8}$$

T_e is the kinetic energy operator for the photoelectron. H_s is the many-body Hamiltonian for the solid. V_{es} is the Coulomb potential between a photoelectron and electrons in the solid. $\boldsymbol{r}$ stands for the photoelectron coordinate. The index i and α label the sites of the electron and those of the nuclear in the solid. $\boldsymbol{r}_i$ and $\boldsymbol{r}_\alpha$ denote the electron and nuclear coordinates in the solid.

Let us introduce some auxiliary expressions for the Hamiltonian in Equation (2.7) given by

$$H = H_s + h_{n^*} + V_{n^*} \tag{2.9}$$

with

$$\begin{aligned} h_{n^*} &= T_e + \langle n^* | V_{es} | n^* \rangle \\ V_{n^*} &= V_{es} - \langle n^* | V_{es} | n^* \rangle \end{aligned} \tag{2.10}$$

where $|n^*\rangle$ correlated target wave function for electrons in the solid is the eigenstate state of H_s in Equation (2.9). V_{n^*} is the interaction between the target with the state $|n^*\rangle$ and the photoelectron.

We write the final state $\Psi^-_{n\boldsymbol{k}}$ in Equation (2.5),

$$|\Psi^-_{n\boldsymbol{k}}\rangle = |n^*\rangle |\phi^-_{\boldsymbol{k}}\rangle + \frac{1}{E - H - i\eta} V_{n^*} |n^*\rangle |\phi^-_{\boldsymbol{k}}\rangle \qquad (\eta \to 0), \tag{2.11}$$

where η is a positive infinitesimal. Since we neglect the identity of a photoelectron with electrons in the target (Blue Electron Theory), we can treat $|\Psi^-_{n\boldsymbol{k}}\rangle$ as the direct product of $|\phi^-_{\boldsymbol{k}}\rangle$ the scattering state of a photoelectron and $|n^*\rangle$ the target state after the photoelectron has left. $|\phi^-_{\boldsymbol{k}}\rangle$ satisfies outgoing-wave boundary conditions

$$h_{n^*} |\phi^-_{\boldsymbol{k}}\rangle = \epsilon_{\boldsymbol{k}} |\phi^-_{\boldsymbol{k}}\rangle , \tag{2.12}$$

where $\epsilon_{\boldsymbol{k}}$ is the free-particle energy of the photoelectron $\hbar^2 k^2/2m$. Note that the hamiltonian h_{n^*} is Hermite so it gives real eigenvalue. We can then rewrite $T(n^*\boldsymbol{k}, 0)$ of Equation (2.5) as

$$\begin{aligned} T(n^*\boldsymbol{k}, 0) &= \langle \phi^-_{\boldsymbol{k}} | \langle n^* | (1 + V_{n^*} G(E)) \Delta | \Psi_0 \rangle , \\ G(E) &= \frac{1}{E - H + i\eta}. \end{aligned} \tag{2.13}$$

To expand the Green's function $G(E)$ in terms of diagonal operators of the Van Hove type [54], We use projection-operator techniques [7] given by

$$\begin{aligned} P &= |n^*\rangle \langle n^*| , \\ Q &= 1 - P. \end{aligned} \tag{2.14}$$

These projection operators satisfy the relation

$$\begin{aligned} P + Q &= 1 \\ PQ &= QP = 0 \\ P^2 &= P, Q^2 = Q. \end{aligned} \tag{2.15}$$

They allows us to write

$$\begin{aligned} V_{n^*} &= (P + Q)V_{n^*}(P + Q) \\ &= PV_{n^*}P + PV_{n^*}Q + QV_{n^*}P + QV_{n^*}Q \\ &= QV_{n^*}Q + QV_{n^*}P + QV_{n^*}Q \end{aligned} \tag{2.16}$$

since $PV_{n^*}P$ is zero

$$\begin{aligned} PV_{n^*}P &= PV_{es}P - P\langle n^*|\, V_{es}\, |n^*\rangle P \\ &= 0. \end{aligned} \tag{2.17}$$

Using these projection operators, we obtain the another expression for the Hamiltonian of Equation (2.9)

$$\begin{aligned} H &= h_{n^*} + H_s + V_{n^*} \\ &= h_{n^*} + H_s + QV_{n^*}Q + QV_{n^*}P + QV_{n^*}Q \\ &= \tilde{H} + \tilde{V} \end{aligned} \tag{2.18}$$

with

$$\begin{aligned} \tilde{H} &= h_{n^*} + H_s + QV_{n^*}Q \\ \tilde{V} &= PV_{n^*}Q + QV_{n^*}P. \end{aligned} \tag{2.19}$$

In Equation (2.19) it trivially follows that

$$\begin{aligned} V_{n^*}\,|n^*\rangle &= (P+Q)V_{n^*}(P+Q)\,|n^*\rangle \\ &= QV_{n^*}P\,|n^*\rangle \\ &= QV_{n^*}P\,|n^*\rangle + PV_{n^*}Q\,|n^*\rangle \\ &= \tilde{V}\,|n^*\rangle\,. \end{aligned} \tag{2.20}$$

We define Green's functions $\tilde{G}$ related to $\tilde{H}$,

$$\tilde{G}(E) = \frac{1}{E-\tilde{H}+i\eta}. \tag{2.21}$$

It satisfies the equations

$$\begin{aligned} Q\tilde{G}P &= P\tilde{G}Q = 0 \\ P\tilde{G}P &= PG_0P \end{aligned} \tag{2.22}$$

with

$$G_0 = \frac{1}{E-h_{n^*}-H_s+i\eta}, \tag{2.23}$$

since it satisfy the identities

$$\begin{aligned} \tilde{G} &= G_0 + G_0QVQ\tilde{G} \\ &= G_0 + \tilde{G}QVQG_0. \end{aligned} \tag{2.24}$$

We rewrite $\langle n^*|\,(1+V_{n^*}G)$ in Equation (2.13) as

$$\begin{aligned} \langle n^*|\,(1+V_{n^*}G) &= \langle n^*|\,(P+Q)(1+V_{n^*}G) \\ &= \langle n^*|\,P(1+V_{n^*}G) \\ &= \langle n^*|\,P(1+\tilde{V}G) \\ &= \langle n^*|\,P(1+\tilde{V}G)P + \langle n^*|\,P(1+\tilde{V}G)Q, \end{aligned} \tag{2.25}$$

since PV_{n^*} equals $P\tilde{V}$, $PV_{n^*} = P\tilde{V}$.

We expand G of Equation (2.13) in powers of $\tilde{V}\tilde{G}$

$$\begin{aligned} G &= \frac{1}{E - \tilde{H} - \tilde{V} + i\eta} \\ &= \frac{1}{\tilde{G}^{-1} - \tilde{V}} \\ &= \frac{\tilde{G}}{1 - \tilde{V}\tilde{G}} \\ &= \tilde{G}(1 + \tilde{V}\tilde{G} + \tilde{V}\tilde{G}\tilde{V}\tilde{G} + ...). \end{aligned} \tag{2.26}$$

This expression for G enable us to rewrite Equation (2.25) as the power series of $\tilde{V}\tilde{G}$. First, we rewrite $P(1 + \tilde{V}G)P$ in the first term as

$$P(1 + \tilde{V}G)P = P(1 + \tilde{V}\tilde{G} + \tilde{V}\tilde{G}\tilde{V}\tilde{G} + ...)P. \tag{2.27}$$

Since the term $P(\tilde{V}\tilde{G})^{2m+1}P, (m = 0, 1...)$ vanishes, we can write $P(1 + \tilde{V}G)P$ as

$$\begin{aligned} &P(1 + \tilde{V}G)P \\ &= P\{1 + (\tilde{V}\tilde{G})^2 + (\tilde{V}\tilde{G})^4 + ...\} \\ &= P\frac{1}{1 - (\tilde{V}\tilde{G})^2}P \\ &= P\frac{1}{1 - \tilde{V}\tilde{G}\tilde{V}\tilde{G}}P \\ &= P\frac{1}{(\tilde{G}^{-1} - \tilde{V}\tilde{G}\tilde{V})\tilde{G}}P \\ &= P\frac{\tilde{G}^{-1}}{\tilde{G}^{-1} - \tilde{V}\tilde{G}\tilde{V}}P \\ &= P\tilde{G}^{-1}\frac{1}{E - \tilde{H} + i\eta - \tilde{V}\tilde{G}\tilde{V}}P \\ &= P\tilde{G}^{-1}(P + Q)\frac{1}{E - \tilde{H} - \tilde{V}\tilde{G}\tilde{V} + i\eta}P \\ &= P\tilde{G}^{-1}P\frac{1}{E - \tilde{H} - \tilde{V}\tilde{G}\tilde{V} + i\eta}P + \underline{P\tilde{G}^{-1}Q}\frac{1}{E - \tilde{H} - \tilde{V}\tilde{G}\tilde{V} + i\eta}P \\ &= P(E - \tilde{H} + i\eta)P\frac{1}{E - \tilde{H} - \tilde{V}\tilde{G}\tilde{V} + i\eta}P \\ &= P(E - \tilde{H} + i\eta)PP\frac{1}{E - \tilde{H} - \tilde{V}\tilde{G}\tilde{V} + i\eta}P, \end{aligned} \tag{2.28}$$

where the underlined terms vanish. We can write the term $P(E-\tilde{H}+i\eta)P$ as

$$\begin{aligned} P(E-\tilde{H}+i\eta)P &= |n^*\rangle\langle n^*|\,(E-H_s-h_{n^*}-QV_{n^*}Q+i\eta)\,|n^*\rangle\langle n^*| \\ &= |n^*\rangle\langle n^*|\,(E-E_{n^*}-h_{n^*}-QV_{n^*}Q+i\eta)\,|n^*\rangle\langle n^*|\,, \\ &= P(\epsilon_{\boldsymbol{k}}-h_{n^*}+i\eta)P. \end{aligned} \tag{2.29}$$

where $E = E_{n^*}+\epsilon_{\boldsymbol{k}}$. We can write the term $P\dfrac{1}{E-\tilde{H}-\tilde{V}\tilde{G}\tilde{V}+i\eta}P$ as

$$\begin{aligned} P\frac{1}{E-\tilde{H}-\tilde{V}\tilde{G}\tilde{V}+i\eta}P &= P\frac{1}{E-E_{n^*}-h_{n^*}-QV_{n^*}Q-\tilde{V}\tilde{G}\tilde{V}+i\eta}P \\ &= P\frac{1}{\epsilon_{\boldsymbol{k}}-h_{n^*}-\tilde{V}\tilde{G}\tilde{V}-i\eta}P. \end{aligned} \tag{2.30}$$

Second, we rewrite $P\tilde{V}\tilde{G}Q$ in the second term of Equation (2.25) as

$$\begin{aligned} P\tilde{V}\tilde{G}Q &= P\tilde{V}(\tilde{G}\tilde{G}\tilde{V}\tilde{G}+...)Q \\ &= P(\tilde{V}\tilde{G}+(\tilde{V}\tilde{G})^2+(\tilde{V}\tilde{G})^3+...)Q. \end{aligned} \tag{2.31}$$

Since the term $P(\tilde{V}\tilde{G})^{2m}Q, (m=1,2,...)$ vanishes, we can write $P\tilde{V}\tilde{G}Q$ as

$$\begin{aligned} P\tilde{V}\tilde{G}Q &= P(1+(\tilde{V}\tilde{G})^2+(\tilde{V}\tilde{G})^4+...)Q \\ &= P\tilde{V}\tilde{G}\frac{1}{1-\tilde{V}\tilde{G}\tilde{V}\tilde{G}}Q \\ &= P\frac{1}{1-\tilde{V}\tilde{G}\tilde{V}\tilde{G}}\tilde{V}\tilde{G}Q \\ &= P\frac{\tilde{G}^{-1}}{\tilde{G}^{-1}-\tilde{V}\tilde{G}\tilde{V}}\tilde{V}\tilde{G}Q \\ &= P\tilde{G}^{-1}\frac{1}{\tilde{G}^{-1}-\tilde{V}\tilde{G}\tilde{V}}\tilde{V}\tilde{G}Q \\ &= P\tilde{G}^{-1}P\frac{1}{\tilde{G}^{-1}-\tilde{V}\tilde{G}\tilde{V}}\tilde{V}\tilde{G}Q+\underline{P\tilde{G}^{-1}Q}\frac{1}{\tilde{G}^{-1}-\tilde{V}\tilde{G}\tilde{V}}\tilde{V}\tilde{G}Q \\ &= P\tilde{G}^{-1}P\frac{1}{\tilde{G}^{-1}-\tilde{V}\tilde{G}\tilde{V}}P\tilde{V}\tilde{G}Q+P\tilde{G}^{-1}P\frac{1}{\tilde{G}^{-1}-\tilde{V}\tilde{G}\tilde{V}}\underline{Q\tilde{V}\tilde{G}Q} \\ &= P(\epsilon_{\boldsymbol{k}}-h_{n^*}+i\eta)\frac{1}{\epsilon_{\boldsymbol{k}}-h_{n^*}-\tilde{V}\tilde{G}\tilde{V}+i\eta}\tilde{V}\tilde{G}Q. \end{aligned} \tag{2.32}$$

From Equation (2.30) and Equation (2.32), we have

$$\begin{aligned}
\langle n^*|\, P(1+\tilde{V}G) &= \langle N^*|\,\{P(1+\tilde{V}G)P + P(1+\tilde{V}G)Q\} \\
&= \langle n^*|\,(\epsilon_{\boldsymbol{k}} - h_{n^*} + i\eta)\frac{1}{\epsilon_{\boldsymbol{k}} - h_{n^*} - \tilde{V}\tilde{G}\tilde{V} + i\eta}(P + \tilde{V}\tilde{G}Q) \\
&= \langle n^*|\,(\epsilon_{\boldsymbol{k}} - h_{n^*} + i\eta)\frac{1}{\epsilon_{\boldsymbol{k}} - h_{n^*} - \Sigma_{n^*}(E) + i\eta}(P + \tilde{V}\tilde{G}Q) \\
&= \langle n^*|\,(\epsilon_{\boldsymbol{k}} - h_{n^*} + i\eta)\frac{1}{\epsilon_{\boldsymbol{k}} - h_{n^*} - \Sigma_{n^*}(E) + i\eta}(1 + \tilde{V}\tilde{G}(P+Q)) \\
&= \langle n^*|\,(\epsilon_{\boldsymbol{k}} - h_{n^*} + i\eta)\frac{1}{\epsilon_{\boldsymbol{k}} - h_{n^*} - \Sigma_{n^*}(E) + i\eta}(1 + \tilde{V}\tilde{G}).
\end{aligned} \tag{2.33}$$

with

$$\begin{aligned}
\Sigma_{n^*}(E) &= \langle n^*|\,\tilde{V}\tilde{G}(E)\tilde{V}\,|n^*\rangle \\
&= \langle n^*|\,\tilde{V}Q\tilde{G}(E)Q\tilde{V}\,|n^*\rangle \\
&= \sum_{m\neq n}\sum_{m'\neq n}\langle n^*|\,\tilde{V}\,|m^*\rangle\,\langle m^*|\,\tilde{G}\,|m'^*\rangle\,\langle m'^*|\,\tilde{V}\,|n^*\rangle
\end{aligned} \tag{2.34}$$

$\Sigma_{n^*}(E)$ is the optical potential [10]. It operate on the photoelectron state $|\phi_{\boldsymbol{k}}\rangle$, but don't operate on the solid state $|n^*\rangle$.

We thus obtain a expression for the transition matrix of Equation (2.13),

$$
\begin{aligned}
T(n^*\boldsymbol{k},0) &= \langle\phi_{\boldsymbol{k}}^-|\langle n^*|(1+V_{n^*}G)\Delta|\Psi_0\rangle \\
&= \langle\phi_{\boldsymbol{k}}^-|\langle n^*|(1+\tilde{V}G)\Delta|\Psi_0\rangle \\
&= \langle\phi_{\boldsymbol{k}}^-|\langle n^*|(\epsilon_{\boldsymbol{k}}-h_{n^*}+i\eta)\frac{1}{\epsilon_{\boldsymbol{k}}-h_{n^*}-\Sigma_{n^*}(E)+i\eta}(1+\tilde{V}\tilde{G})\Delta|\Psi_0\rangle \\
&= \langle\phi_{\boldsymbol{k}}^-|(\epsilon_{\boldsymbol{k}}-h_{n^*}+i\eta)\frac{1}{\epsilon_{\boldsymbol{k}}-h_{n^*}-\Sigma_{n^*}(E)+i\eta}\langle n^*|(1+\tilde{V}\tilde{G})\Delta|\Psi_0\rangle \\
&= i\eta\langle\phi_{\boldsymbol{k}}^-|\frac{1}{\epsilon_{\boldsymbol{k}}-h_{n^*}-\Sigma_{n^*}(E)+i\eta}\langle n^*|(1+\tilde{V}\tilde{G})\Delta|\Psi_0\rangle \\
&= \langle\phi_{\boldsymbol{k}}^-|(\epsilon_{\boldsymbol{k}}-h_{n^*}-\Sigma_{n^*}(E)+i\eta)\frac{1}{\epsilon_{\boldsymbol{k}}-h_{n^*}-\Sigma_{n^*}(E)+i\eta}\langle n^*|(1+\tilde{V}\tilde{G})\Delta|\Psi_0\rangle \\
&\quad -\langle\phi_{\boldsymbol{k}}^-|(\epsilon_{\boldsymbol{k}}-h_{n^*}-\Sigma_{n^*})\frac{1}{\epsilon_{\boldsymbol{k}}-h_{n^*}-\Sigma_{n^*}(E)+i\eta}\langle n^*|(1+\tilde{V}\tilde{G})\Delta|\Psi_0\rangle \\
&= \langle\phi_{\boldsymbol{k}}^-|\langle n^*|(1+\tilde{V}\tilde{G})\Delta|\Psi_0\rangle \\
&\quad +\langle\phi_{\boldsymbol{k}}^-|\Sigma_{n^*}\frac{1}{\epsilon_{\boldsymbol{k}}-h_{n^*}-\Sigma_{n^*}(E)+i\eta}\langle n^*|(1+\tilde{V}\tilde{G})\Delta|\Psi_0\rangle \\
&= \langle\phi_{\boldsymbol{k}}^-|\left\{1+\Sigma_{n^*}\frac{1}{\epsilon_{\boldsymbol{k}}-h_{n^*}-\Sigma_{n^*}(E)+i\eta}\right\}\langle n^*|(1+\tilde{V}\tilde{G})\Delta|\Psi_0\rangle \\
&= \langle\psi_{\boldsymbol{k}}^-|\langle n^*|(1+\tilde{V}\tilde{G})\Delta|\Psi_0\rangle\,,
\end{aligned}
\tag{2.35}
$$

with

$$
\begin{aligned}
|\psi_{\boldsymbol{k}}^-\rangle &= \left(1+\frac{1}{\epsilon_{\boldsymbol{k}}-h_{n^*}-\Sigma_{n^*}^\dagger-i\eta}\Sigma_{n^*}\right)|\phi_{\boldsymbol{k}}^-\rangle \\
&= |\phi_{\boldsymbol{k}}^-\rangle+\frac{1}{\epsilon_{\boldsymbol{k}}-h_{n^*}-\Sigma_{n^*}^\dagger-i\eta}\Sigma_{n^*}^\dagger|\phi_{\boldsymbol{k}}^-\rangle\,.
\end{aligned}
\tag{2.36}
$$

$|\psi_{\boldsymbol{k}}^-\rangle$ is the damped wave function for a photoelectron.

We acquired another expression for $T(n^*\boldsymbol{k},0)$ in Equation (2.35) by rearranging the perturbation expansion in V to make the state $|\Psi_{n^*}\rangle$ forbid to appear as an intermediate state. We replace the undamped wave function $|\phi_{\boldsymbol{k}}^-\rangle$ and the green function G in Equation (2.13) by a damped wave function $|\psi_{\boldsymbol{k}}^-\rangle$ and $\tilde{G}$ in Equation (2.35). Photoelectron waves attenuate as they propagate under the influence of the optical potential Σ_{n^*}, which is the complex potential and is an imaginary constant inside the solid and zero outside in the lowest approximation.

We can write the electron-phonon interaction Δ in Equation (2.35) as [55],

$$\Delta = \sum_{i,j} \langle i| \Delta |j\rangle \, c_i^\dagger c_j, \tag{2.37}$$

where the indices i and j labels the states of the electron. $\langle i| \Delta |j\rangle$ is a optical transition matrix. c_j is the annihilation operator of the one-electron state $|j\rangle$, and $c_i^\dagger$ is the creation operator of the state $|i\rangle$.

For a core level photoemission,

1. we can regard the state $|i\rangle$ as a one-electron excited state *ketk* (When the photo-electron k is fast enough comparing to the sounding electrons, there are no virtual states i in $|\Psi_0\rangle$ to annihilate) and

2. $|j\rangle$ describes a one-electron core state $|c\rangle$ from which a photoelectron is excited.

We then obtain the Δ for a core level photoemission

$$\Delta = \sum_{k} \langle k| \Delta |c\rangle \, c_k^\dagger b, \tag{2.38}$$

where b and $b^\dagger$ are the annihilation and creation operator of the core state ϕ_c. We can then write $\Delta |\Psi_0\rangle$ in Equation (2.35) as

$$\begin{aligned} \Delta |\Psi_0\rangle &= \sum_{k} \langle k| \Delta |c\rangle \, c_k^\dagger b |\Psi_0\rangle \\ &= \sum_{k} \langle k| \Delta |c\rangle \, |k\rangle \, b |\Psi_0\rangle \\ &= \sum_{k} |k\rangle \langle k| \Delta |c\rangle \, b |\Psi_0\rangle \\ &\sim \Delta |c\rangle \, b |\Psi_0\rangle \, , \end{aligned} \tag{2.39}$$

which is approximated by $\sum_k |k\rangle \langle k| \sim 1$.

We obtain the expression for $T(n^*\boldsymbol{k}, 0)$ in Equation (2.35)

$$\begin{aligned} T(n^*\boldsymbol{k}, 0) &\sim \langle \psi_{\boldsymbol{k}}^-| \langle n^*| (1 + \tilde{V}\tilde{G}) b |\Psi_0\rangle \, \Delta |c\rangle \\ &= \langle \psi_{\boldsymbol{k}}^-| \, \Delta |c\rangle \, \langle n^*|b|\Psi_0\rangle + \langle \psi_{\boldsymbol{k}}^-| \langle n^*| \, \tilde{V}\tilde{G} b |\Psi_0\rangle \, \Delta |c\rangle \\ &= \langle \psi_{\boldsymbol{k}}^-| \, \Delta |c\rangle \, \langle n^*|b|0\rangle + \langle \psi_{\boldsymbol{k}}^-| \langle n^*| \, \tilde{V}\tilde{G} b |0\rangle \, \Delta |c\rangle \, , \end{aligned} \tag{2.40}$$

where $|\Psi_0\rangle$ stands for $|0\rangle$. We can obtain simple expression for Equation (2.40) by inserting $\sum l\,|l^*\rangle\langle l^*| = 1$ before the annihilation operator b,

$$\begin{aligned} T(n^*\boldsymbol{k},0) &= \langle\psi_{\boldsymbol{k}}^-|\,\Delta\,|c\rangle\,\langle n^*|b|0\rangle + \sum_l \langle\psi_{\boldsymbol{k}}^-|\,\langle n^*|\,\tilde{V}\tilde{G}\,|l^*\rangle\,\langle l^*|\,b\,|0\rangle\,\Delta\,|c\rangle \\ &= \langle\psi_{\boldsymbol{k}}^-|\,\Delta\,|c\rangle\,S_n + \sum_l \langle\psi_{\boldsymbol{k}}^-|\,\langle n^*|\,\tilde{V}\tilde{G}\,|l^*\rangle\,\Delta\,|c\rangle\,S_l \end{aligned} \tag{2.41}$$

with

$$S_n = \langle n^*|\,b\,|0\rangle\,(n = 0, 1, 2...). \tag{2.42}$$

We name S_n intrinsic amplitude, which describes the process that the core electron is ejected from a core level. The transition matrix $T(n^*\boldsymbol{k},0)$ represents the photoemission process including energy losses by plasmon excitation. The formula indicate: in the first term in Equation (2.41), the plasmon excitation, transmission from the state without plasmon to that with plasmon, occurs only in the intrinsic process S_n, and in the second term, the plasmon excitation occurs in the extrinsic process $\langle n^*|\,\tilde{V}\tilde{G}\,|l^*\rangle$ after the intrinsic process S_l. The final state of the solid should be $|n^*\rangle$, no matter what process $\tilde{V}\tilde{G}$ is taken between the initial state $|l^*\rangle$ and the final state. That extrinsic process contains the cases of virtual transition.

In the case that $n^* = 0^*$, the transition matrix corresponds to a main peak of core level photoemission. It is given by

$$\begin{aligned} T(0^*\boldsymbol{k},0) &= \langle\psi_{\boldsymbol{k}}^-|\,\Delta\,|c\rangle\,S_0 + \sum_l \langle\psi_{\boldsymbol{k}}^-|\,\langle 0^*|\,\tilde{V}\tilde{G}\,|l^*\rangle\,\Delta\,|c\rangle\,S_l \\ &\sim \langle\psi_{\boldsymbol{k}}^-|\,\Delta\,|c\rangle\,S_0 \end{aligned} \tag{2.43}$$

There is no plasmon excitation in the first term in Equation (2.43). The second term means one excitation takes place in the intrinsic process S_l, and deexcitation in extrinsic process $\langle 0^*|\,\tilde{V}\tilde{G}\,|l^*\rangle$. The plasmon excitation makes the amplitudes of photoelectrons reduced, therefore the term that contains one excitation and dexcitaion is rather smaller than the first term, so it can be neglected.

To obtain new expression for the second term in $T(n^*\boldsymbol{k},0)$ of Equation (2.41), we introduce the

expansion in diagonal Green functions [8, 10]. Consider a Hamiltonian,

$$H = H_0 + V \tag{2.44}$$

with

$$\begin{aligned} H_0 &= h_{n^*} + H_s + \sum_l P_l V_{es} P_l \\ V &= V_{es} - \sum_l P_l V_{es} P_l, \end{aligned} \tag{2.45}$$

where the diagonal elements of V with respect to eigenstate of H_0 are zero, $\langle i| H |i\rangle = 0$. We introduce a complement Q_{ij} of a set of projection operator

$$Q_{ij} = 1 - P_i - P_j. \tag{2.46}$$

We define the truncated potential $Q_i V Q_i$

$$V_i = Q_i V Q_i. \tag{2.47}$$

$Q_i V Q_i$ is written by Q_{ij}

$$\begin{aligned} V_i = Q_i V Q_i &= (Q_{ij} + P_i) V (Q_{ij} + P_i) \\ &= Q_{ij} V Q_{ij} + P_i V Q_{ij} + Q_{ij} V P_j \\ &= Q_{ij} V Q_{ij} + \tilde{V}_{ij}. \end{aligned} \tag{2.48}$$

We define Green's functions

$$\begin{aligned} G_i &= \frac{1}{E - H_0 - Q_i V Q_i + i\eta} \\ G_{\bar{i}} &= \frac{Q_i}{E - H_0 - Q_i V Q_i + i\eta} \end{aligned} \tag{2.49}$$

and

$$\begin{aligned} G_{ij} &= \frac{1}{E - H_0 - Q_{ij} V Q_{ij} + i\eta} \\ G_{\bar{i}\bar{j}} &= \frac{Q_{ij}}{E - H_0 - Q_{ij} V Q_{ij} + i\eta}. \end{aligned} \tag{2.50}$$

By projection-operator techniques $G_{\bar{i}} |j\rangle$ is written as,

$$\begin{aligned} G_{\bar{i}} |j\rangle &= Q_i \frac{1}{E - H_0 - Q_i V Q_i + i\eta} |j\rangle \\ &= (P_j + Q_{ij}) \frac{1}{E - H_0 - Q_{ij} V Q_{ij} - \tilde{V}_{ij} + i\eta} |j\rangle \\ &= (P_j + Q_{ij})(G_{ij} + G_{ij}\tilde{V}_{ij}G_{ij} + G_{ij}\tilde{V}_{ij}G_{ij}\tilde{V}_{ij}G_{ij} + ...)P_j |j\rangle \\ &= P_j G_{ij}(1 + (\tilde{V}_{ij}G_{ij})^2 + ...)P_j |j\rangle + Q_{ij}G_{ij}\tilde{V}_{ij}G_{ij}(1 + (\tilde{V}_{ij}G_{ij})^2 + ...)P_j |j\rangle \\ &= (P_j + Q_{ij}G_{ij}\tilde{V}_{ij})G_{ij} \frac{1}{1 - \tilde{V}_{ij}G_{ij}\tilde{V}_{ij}G_{ij}} P_j |j\rangle \\ &= (P_j + Q_{ij}G_{ij}\tilde{V}_{ij}) \frac{1}{G_{ij}^{-1} - \tilde{V}_{ij}G_{ij}\tilde{V}_{ij}} P_j |j\rangle \\ &= (P_j + Q_{ij}G_{ij}\tilde{V}_{ij}) \frac{1}{E - H_0 - \tilde{V}_{ij}G_{ij}\tilde{V}_{ij} - Q_{ij}VQ_{ij} + i\eta} P_j |j\rangle \\ &= (P_j + Q_{ij}G_{ij}\tilde{V}_{ij})P_j \frac{1}{E - H_0 - \tilde{V}_{ij}G_{ij}\tilde{V}_{ij} - Q_{ij}VQ_{ij} + i\eta} P_j |j\rangle \\ &= (1 + G_{\bar{i}\bar{j}}\tilde{V}_{ij})P_j \frac{1}{E - H_0 - \Sigma_{ij}(E) - Q_{ij}VQ_{ij} + i\eta} |j\rangle \\ &= (1 + G_{\bar{i}\bar{j}}\tilde{V}_{ij})(P_i + Q_i)P_j \frac{1}{E - H_0 - \Sigma_{ij}(E) - Q_{ij}VQ_{ij} + i\eta} |j\rangle \\ &= (1 + G_{\bar{i}\bar{j}}\tilde{V}_{ij})Q_i P_j \frac{1}{E - H_0 - \Sigma_{ij}(E) - Q_{ij}VQ_{ij} + i\eta} |j\rangle \\ &= (1 + G_{\bar{i}\bar{j}}\tilde{V}_{ij})G_{ij}^d(E) |j\rangle \end{aligned} \tag{2.51}$$

where

$$\begin{aligned} G^d_{ij}(E) &= Q_i P_j \frac{1}{E - H_0 - \Sigma_{ij}(E) - Q_{ij} V Q_{ij} + i\eta} \\ &= P_j \frac{1}{E - H_0 - \Sigma_{ij}(E) - Q_{ij} V Q_{ij} + i\eta} \end{aligned} \tag{2.52}$$

with

$$\begin{aligned} \Sigma_{ij}(E) &= \langle j | \, \tilde{V}_{ij} G_{0j} \tilde{V}_{ij} \, | j \rangle \\ &= \langle j | \, V Q_{ij} G_{0j} V \, | j \rangle \\ &= \langle j | \, V G_{\bar{0}j} V \, | j \rangle \, . \end{aligned} \tag{2.53}$$

G^d_{ij} is a diagonal Green's function and $\Sigma_{ij}(E)$ is a self energy. The self-energy provides a shift in energy and some damping in the coherent propagation.

From the identities in Equation (2.24), we obtain another expression for diagonal Green's function

$$\begin{aligned} G^d_{ij} &= Q_i P_j G_0 + Q_i P_j G_0 (Q_{ij} V Q_{ij} + \Sigma_{ij}(E)) G_{ij} \\ &= Q_i P_j G_0 + Q_i P_j G_0 \Sigma_{ij}(E) G_{ij} \\ &= Q_i P_j \frac{1}{E - H_0 - \Sigma_{ij}(E) + i\eta}. \end{aligned} \tag{2.54}$$

Using the identity, an expansion in terms of diagonal Green's function is derived,

$$\begin{aligned} G_{\bar{i}} \, | j \rangle &= G^d_{ij}(E) \, | j \rangle + G_{\bar{i}\bar{j}} \tilde{V}_{ij} G^d_{ij}(E) \, | j \rangle \\ &= G^d_{ij}(E) \, | j \rangle + \sum_{k \neq i,j} Q_{ij} G_{ij} \, | k \rangle \langle k | \, V P_j G^d_{ij}(E) \, | j \rangle \\ &= G^d_{ij}(E) \, | j \rangle + \sum_{k \neq i,j} G^d_{ijk} \langle k | \, V \, | j \rangle \, G^d_{ij}(E) \, | j \rangle + ... \end{aligned} \tag{2.55}$$

The same intermediate state can never appear more than once. Taking a particular term in this expansion, the same intermediate state can never appear more than once.

We have discussed the expansion of diagonal Green's function. $T(n^*\boldsymbol{k}, 0)$ in Equation (2.43) is then written by,

$$\begin{aligned} T(n^*\boldsymbol{k}, 0) &= \langle\psi^-_{\boldsymbol{k}}|\,\Delta\,|c\rangle\, S_n + \langle\psi^-_{\boldsymbol{k}}|\,\langle n^*|\,\tilde{V}\tilde{G}\,|0^*\rangle\,\Delta\,|c\rangle\, S_0 + \sum_{l\neq 0}\langle\psi^-_{\boldsymbol{k}}|\,\langle n^*|\,\tilde{V}\tilde{G}\,|l^*\rangle\,\Delta\,|c\rangle\, S_l \\ &\sim \langle\psi^-_{\boldsymbol{k}}|\,\Delta\,|c\rangle\, S_n + \langle\psi^-_{\boldsymbol{k}}|\,\langle n^*|\,\tilde{V}\tilde{G}\,|0^*\rangle\,\Delta\,|c\rangle\, S_0, \end{aligned} \tag{2.56}$$

where we ignore the third term which considers excitations in the intrinsic process S_l and extrinsic process $\langle n^*|\,\tilde{V}\tilde{G}\,|l^*\rangle$. The second term is written by,

$$\begin{aligned} \langle n^*|\,\tilde{V}\tilde{G}\,|0^*\rangle &= \langle n^*|\,\tilde{V}(P+Q)\tilde{G}\,|0^*\rangle \\ &= \langle n^*|\,\tilde{V}Q\tilde{G}\,|0^*\rangle \\ &= \langle n^*|\,V_{n^*}Q\tilde{G}\,|0^*\rangle \\ &= \langle n^*|\,V_{n^*}G^d_{nl}(E)\,|0^*\rangle + \sum_{p\neq n,0}\langle n^*|\,V_{n^*}\,|p^*\rangle\, G^d_{n0p}\,\langle p^*|\,V_{n^*}\,|0^*\rangle\, G^d_{n0}(E)\,|0^*\rangle + ... \\ &\sim \langle n^*|\,V_{n^*}G^d_{n0}(E)\,|0^*\rangle\,. \end{aligned} \tag{2.57}$$

We can obtain the simple expression for the diagonal Green's function in Equation (2.54)

$$\begin{aligned} G^d_{n0}(E) &= P_0\frac{1}{E - H_0 - \Sigma_{n0}(E) + i\eta} \\ &= \frac{1}{E - H_0 - \Sigma_{n0}(E) + i\eta}\,|0^*\rangle\,\langle 0^*| \\ &= \frac{1}{E - h_{n^*} - H_s - \Sigma_{n0}(E) + i\eta}\,|0^*\rangle\,\langle 0^*| \\ &= \frac{1}{E - h_{n^*} - E_{0^*} - \Sigma_{n0}(E) + i\eta}\,|0^*\rangle\,\langle 0^*| \\ &= \frac{1}{E - h_{n^*} - E_{0^*} - \Sigma_0(E - E_{0^*}) + i\eta}\,|0^*\rangle\,\langle 0^*| \\ &= \frac{1}{\epsilon_{\boldsymbol{k}} + E_{n^*} - h_{n^*} - E_{0^*} - \Sigma_0(\epsilon_{\boldsymbol{k}} + E_{n^*} - E_{0^*}) + i\eta}\,|0^*\rangle\,\langle 0^*| \\ &= \frac{1}{\epsilon_{\boldsymbol{k}} + \omega_n - h_{n^*} - \Sigma_0(\epsilon_{\boldsymbol{k}} + \omega_n) + i\eta}\,|0^*\rangle\,\langle 0^*| \\ &= g(\epsilon_{\boldsymbol{k}} + \omega_n) \end{aligned} \tag{2.58}$$

with

$$g(\epsilon) = \frac{1}{\epsilon - h - \Sigma_0(\epsilon) + i\eta}. \tag{2.59}$$

where $g(\epsilon)$ is one-electron green function and we labeled $h = h_{n^*}$. We note that $E = \omega + E_0 = \epsilon_{\boldsymbol{k}} + E_{n^*}$ and $\omega_n = E_{n^*} - E_{0^*}$.

We obtain the expression for the transition matrix $T(m^*\boldsymbol{k}, 0)$ in the case of single plasmon loss excitation $n^* = m^*$ (n denotes for the excitation state and m denotes for the boson mode)

$$T(m^*\boldsymbol{k}, 0) \sim \langle\psi_{\boldsymbol{k}}^-|\,\Delta\,|\phi_c\rangle\, S_{m^*} + \langle\psi_{\boldsymbol{k}}^-|\,\langle m^*|\,V_{m^*}\,|0^*\rangle\, g(\epsilon_{\boldsymbol{k}} + \omega_m)\Delta\,|\phi_c\rangle\, S_{0^*} \tag{2.60}$$

2.1.2 No loss Intensity

The intensity of no plasmon loss without energy loss is described by the transition matrix $T(0^*\boldsymbol{k}, 0)$ in Equation (2.43). The virtual loss by the optical potential occurs in this transition without energy loss. In the virtual loss, the amplitude of photoelectron wave damps and it means the number of the photoelectrons, that is their intensity, damps. Therefore in the calculation $T(0^*\boldsymbol{k}, 0)$, we should take into account not only ordinary potential scattering corresponding to elastic scattering but also damping effect by the optical potential.

Main XPS peak (no plasmon loss peak) measuring photoelectrons with momentum $\boldsymbol{k}$ excited by X-ray photons with energy ω is given by,

$$\begin{aligned} I(\boldsymbol{k}, \omega)_c^0 &= 2\pi|T(0^*\boldsymbol{k}, 0)|^2\delta(E_0 + \omega - E_0^* - \epsilon_{\boldsymbol{k}}) \\ T(0^*\boldsymbol{k}, 0) &= \langle\psi_{\boldsymbol{k}}^-|\Delta|\phi_c\rangle S_0. \end{aligned} \tag{2.61}$$

The ground state energies with and without core hole are E_0^* and E_0. S_0 is intrinsic amplitude defined in Equation (2.42) and it will be discussed in section 2.1.3. The photoelectron wave amplitude $\langle\psi_{\boldsymbol{k}}^-|\Delta|\phi_{c_A}\rangle$ can be calculated by full multiple scattering formula in photoelectron diffraction [56, 57, 58]. The derivation of the photoelectron wave amplitude acquires to consider the optical potential, which is a complex potential. We follow the Fujikawa, Shinotsuka method to calculate the photoelectron wave amplitude.

T matrix expansion with the complex optical potential

In the previous section 2.1, we discussed how the damping scattering waves $|\psi_p^-\rangle$ is given in Equation (2.36). The damping scattering wave function for the photoelectron without energy loss ($n^* = 0^*$) is given by,

$$\begin{aligned} |\psi_{\boldsymbol{k}}^-\rangle &= |\phi_{\boldsymbol{k}}^-\rangle + \frac{1}{\epsilon - h_{0^*} - \Sigma_{0_*} + i\eta}\Sigma_{0_*}|\phi_{\boldsymbol{k}}^-\rangle \\ &= |\phi_{\boldsymbol{k}}^-\rangle + \frac{1}{\epsilon - T_e - \langle 0^*|V_{es}|0^*\rangle - \Sigma_{0_*} + i\eta}\Sigma_{0_*}|\phi_{\boldsymbol{k}}^-\rangle\,. \end{aligned} \tag{2.62}$$

$\langle 0^*|V_{es}|0^*\rangle$ is the Hartree (Coulomb) potential V_H and Σ_{0_*} is the nonlocal optical potential Σ. Since the optical potential is non-Hermite, it has two different parts,

$$\Sigma(\epsilon_k) = Re\Sigma(\epsilon_k) - i\Gamma(\epsilon_k) \tag{2.63}$$

The real (Hermitian) part $Re\Sigma$ has substantial effects on the T-matrix $t_l^\alpha(k)$ (the elastic scattering), and the imaginary (anti-Hermitian) part $-i\Gamma$ is responsible for the photoelectron wave damping which is usually approximated by a constant.

Actually the amplitude is calculated by dividing for each atomic potential in different site. When the potential is given as a sum of non overlapping atomic potential,

$$V = V_H + \Sigma = \sum_\alpha v_\alpha, \tag{2.64}$$

we have two different expressions for the propagator expanded in terms of site T matrix [14],

$$\begin{aligned} g(\epsilon) &= \frac{1}{\epsilon - T_e + \langle 0^*|V_{es}|0^*\rangle - \Sigma_{0_*} + i\eta} \\ &= \frac{1}{\epsilon - T_e - V_H - Re\Sigma + i\Gamma + i\eta} \\ &= g_0 + g_0(V_H + Re\Sigma)g_0 + ... \qquad (2.65) \\ &= \bar{g_0} + \bar{g_0}(V_H + Re\Sigma - i\Gamma)\bar{g_0} + ... \qquad (2.66) \end{aligned}$$

and the free propagators $g_0(\epsilon)$ and $\bar{g_0}(\epsilon)$ are given by,

$$g_0(\epsilon) = \frac{1}{\epsilon - T_e + i\Gamma}, \tag{2.67}$$

$$\bar{g_0}(\epsilon) = \frac{1}{\epsilon - T_e + i\eta}, (\eta \to +0). \tag{2.68}$$

In the first expansion in Equation (2.65), the muffin-tin constant is a real constant value v_0, on the other hand it is $v_0 - i\Gamma$ in the second expansion in terms of $\bar{g_0}$. The former choice gives unperturbed plane wave $\phi^0_{\boldsymbol{k}}$ the complex wave number $\tilde{k}$

$$\tilde{k} = \sqrt{2(\epsilon_k + i\Gamma)} = Re\tilde{k} + i\kappa, (\tilde{k}||k) \tag{2.69}$$

When Γ as a muffin-tin constant is determined and it is small enough in each atomic sphere, the phase shift calculations are only affected by the real potential. In the high-energy region, we have the widely-used formula

$$\kappa \sim \Gamma/k \sim -Im\Sigma/k. \tag{2.70}$$

In the second expansion we cannot reject the redundant scatterings from complex potential $-i\Gamma$ in the interstitial region. Thus we do the first expansion in Equation (2.65).

We apply the site T-matrix expansion for $\psi^-_{\boldsymbol{k}}$,

$$\begin{aligned}\langle\psi^-_{\boldsymbol{k}}|\Delta|\phi_c\rangle &= \langle\phi^-_{\boldsymbol{k}}|(g_A + \sum_\beta g_0\tau_\beta g_A + ...)\Delta|\phi_c\rangle \\ &= \langle\phi^-_{\boldsymbol{k}}|g_A\Delta|\phi_c\rangle + +\langle\phi^-_{\boldsymbol{k}}|\sum_\beta g_0\tau_\beta g_A\Delta|\phi_c\rangle + ... \\ &= Z_1(\boldsymbol{k}) + Z_2(\boldsymbol{k}) + ...\end{aligned} \tag{2.71}$$

where $Z_1(\boldsymbol{k})$ is the amplitude without scatterings from surrounding atoms (direct terms), $Z_2(\boldsymbol{k})$ is the single-scattering amplitude, and so on. The direct term Z_1 is written by

$$\begin{aligned}Z_1(\boldsymbol{k}) &= \langle\phi^-_{A\boldsymbol{k}}|\Delta|\phi_c\rangle \\ &= \sum_L e^{-\kappa D_A(\hat{k})}Y_L(\hat{\boldsymbol{k}})M_{LL_c},\end{aligned} \tag{2.72}$$

where $\phi^-_{A\boldsymbol{k}}$ the photoelectron wave function emitted from an x-ray absorbed atom A, and L is the abbreviated form of the pair of angular momentum, $L = (l, m)$. $D_\alpha(\hat{\boldsymbol{k}})$ is the distance from the site A to the surface of the solid along the direction of a photoelectron propagation $\hat{\boldsymbol{k}}$. $e^{-\kappa D_A(\hat{k})}$ gives the damping of photoelectron. In the dipole approximation, the photoexcitation matrix element M_{LL_c} excited by linearly polarized light parallel to the z axis is given by

$$M_{LL_c} = \sqrt{\frac{2}{\pi}} i^{-l} e^{i\delta^A_l} \rho(l)_c G(L_c 10|L) \tag{2.73}$$

with

$$\rho(l)_c = \int R_l(kr) R_{l_c}(r) r^3 dr. \tag{2.74}$$

where δ^A_l is the phase shift of lth partial wave at site A, and $R_l(kr)$ and $R_{l_c}(r)$ describe the radial part labeled by the orbital angular momentum of $\phi^-_{A\boldsymbol{k}}$ and ϕ_{c_A}, respectively. Gaunt integral $G(L_c 10|L) = \int Y_{L_c}(\boldsymbol{r}) Y_{10}(\boldsymbol{r}) Y^*_L(\boldsymbol{r}) d\hat{\boldsymbol{r}}$ is responsible for the angular momentum selection rule of the photoexcitation. The single-scattering term Z_2 is explicitly written by

$$\begin{aligned} Z_2 &= \sum \langle \phi^0_{\boldsymbol{k}} | t_\alpha g_A \Delta | \phi_c \rangle \\ &= \sum_{\alpha \neq A} e^{-\kappa D_\alpha(\hat{k})} e^{-i\boldsymbol{k}\cdot\boldsymbol{R}_{\alpha A}} \sum_{LL'} Y_{L'}(\hat{\boldsymbol{k}}) t^\alpha_{l'}(k) G_{L'L}(k\boldsymbol{R}_{\alpha A}) e^{-\kappa \boldsymbol{R}_{\alpha A}} M_{LL_c}, \end{aligned} \tag{2.75}$$

$$g_A = g_0 + g_0 t_A g_0 \tag{2.76}$$

where ϕ^0_k is the plane wave and $\boldsymbol{R}_{\alpha A}$ is the position vector of scatterer α measured from a photoelectron emitter A. The angular momentum representation of the site-t matrix $t^\alpha_l(k)$ at site α is given by

$$t^\alpha_l(k) = -\frac{e^{2i\delta^\alpha_l} - 1}{2ik} \tag{2.77}$$

in terms of the phase shift δ^α_l at site α and the photoelectron wave number k. The propagator $G_{L'L}(k\boldsymbol{R}_{\alpha A})$ describes electron propagation from the site A with L to the site α with L'.

In terms of $X = tG$, we are given the general renormalized multiple scattering XPD formula which

contains the damping effects,

$$\langle\psi_{\boldsymbol{k}}^{-}|\Delta|\phi_c\rangle = \sum_{\alpha} e^{-\kappa d_\alpha(\hat{k})} e^{-i\boldsymbol{k}\cdot\boldsymbol{R}_{\alpha A}} \sum_{LL'} Y_{L'}(\hat{\boldsymbol{k}}) \left[(1-X)^{-1}\right]_{LL'}^{\alpha A} M_{LL_c}, \tag{2.78}$$

with

$$X_{LL'}^{\alpha\beta} = t_{l'}^{\alpha}(k) G_{L'L}(k\boldsymbol{R}_{\alpha\beta}) \exp(-\kappa R_{\alpha\beta})(1-\delta_{\alpha\beta}), \tag{2.79}$$

where X is a square matrix, whose element is labeled by a set of atomic sites (A, α, β, ...) and angular momentum L, and matrix$X$ have dimension $N(l_{max}+1)^2$ for the cluster of N atoms and maximum angular momentum l_{max}. We use the inverse matrix $(1-X)^{-1}$ to take into account the full multiple scattering.

2.1.3 Single loss Intensity

The intensity of single plasmon loss is described by the transition matrix $T(m^*\boldsymbol{k}, 0)$ in Equation (2.84). Index m denotes boson mode which describe the state with the plasmon excitation. Transition from 0^* to m^* describes that the process of the excitation which a photoelectron once make a inelastic scattering with electrons in the solid, and transfers energy and momentum to the electrons. During this process, the photoelectron lose a part of its energy ω_m, and this lost energy is given to the electrons in the solid and make it excite. These excitations have two cases: one is that the plasmon excites in the photoelectron photoexcitation process, intrinsic process, and the other is that the plasmon excites in the process of the photoelectron transmission in the solid (it is so called the extrinsic process). Here, we explain how these two process can be described.

We obtained the expression for the transition matrix $T(m^*\boldsymbol{k}, 0)$ in the case of single plasmon loss excitation $n^* = m^*$ (n denotes for the excitation state and m denotes for the boson mode)

$$T(m^*\boldsymbol{k}, 0) \sim \langle\psi_{\boldsymbol{k}}^{-}|\,\Delta\,|\phi_c\rangle\, S_{m^*} + \langle\psi_{\boldsymbol{k}}^{-}|\,\langle m^*|\,V_{m^*}\,|0^*\rangle\, g(\epsilon_{\boldsymbol{k}}+\omega_m)\Delta\,|\phi_c\rangle\, S_{0^*} \tag{2.60}$$

Here, potential V_{nm^*} is written as,

$$\begin{aligned} V_{m^*}(\boldsymbol{r}) &= V_{es} - \langle m^*|\,V_{es}\,|m^*\rangle \\ &= \int v(\boldsymbol{r}-\boldsymbol{r}')\delta\rho_{m^*}(\boldsymbol{r}')d\boldsymbol{r}' \end{aligned} \tag{2.80}$$

with

$$\delta\rho_m(\boldsymbol{r}) = \rho(\boldsymbol{r}) - \langle m|\,\rho(\boldsymbol{r})\,|m\rangle\,. \tag{2.81}$$

The expression for V_{n^*} of Equation (2.80) enable us to rewrite $\langle m^*|\,V_{m^*}\,|0^*\rangle$ in Equation (2.60) as

$$\begin{aligned}\langle m^*|\,V_{m^*}\,|0^*\rangle &= \langle m^*|\left\{\int v(\boldsymbol{r}-\boldsymbol{r}')\delta\rho_{m^*}(\boldsymbol{r}')d\boldsymbol{r}'\right\}|0^*\rangle \\ &= \int v(\boldsymbol{r}-\boldsymbol{r}')\,\langle m^*|\,\delta\rho_{m^*}(\boldsymbol{r}')\,|0^*\rangle\,d\boldsymbol{r}' \\ &= v_{m^*}(\boldsymbol{r}).\end{aligned} \tag{2.82}$$

The fluctuation potential $v_m(\boldsymbol{r})$ is defined by [9, 13]

$$v_m(\boldsymbol{r}) = \int v(\boldsymbol{r}-\boldsymbol{r}')\,\langle m|\,\delta\rho_m(\boldsymbol{r}')\,|0\rangle\,d\boldsymbol{r}'. \tag{2.83}$$

We can regard $v_{m^*}(\boldsymbol{r})$ as $v_m(\boldsymbol{r})$ in Equation (2.82) [9]. Thus, we obtain $T(m^*\boldsymbol{k},0)$,

$$T(m^*\boldsymbol{k},0) = \langle\psi^-_{\boldsymbol{k}}|\,\Delta\,|\phi_c\rangle\,S_m + \langle\psi^-_{\boldsymbol{k}}|\,v_m g(\epsilon_{\boldsymbol{k}}+\omega_m)\Delta\,|\phi_c\rangle\,S_0 \tag{2.84}$$

Single-loss XPS intensity, whose loss energy is ω_m, is written by Equation (2.60),

$$\begin{aligned}I(\boldsymbol{k};\omega)^1 &= 2\pi\sum_m |T(m^*\boldsymbol{k},0)|^2\delta(E_0+\omega-E_0^*-\omega_m-\varepsilon_k) \\ T(0^*\boldsymbol{k},0) &= \langle\psi^-_{\boldsymbol{k}}|\Delta|\phi_c\rangle S_m + \langle\psi^-_{\boldsymbol{k}}|v_m g(\varepsilon_k+\omega_m)\Delta|\phi_c\rangle S_0\end{aligned} \tag{2.85}$$

where v_m is the fluctuation potential defined in Equation (2.83). It gives amplitude for the terms of extrinsic and intrinsic plasmon excitations.

Here, we show how intrinsic amplitudes S_0, S_m $(m = 0, 1, 2...)$ in Equation (2.42) are given. We introduce quasi-boson Hamiltonian [6],

$$H = H_v + \varepsilon_c b^\dagger b + V_c b b^\dagger. \tag{2.86}$$

H_v is a full many-electron Hamiltonian for valence electrons, V_c is an interaction between a core-hole and valence electrons, and ε_c is a core electron energy. The solid state without core hole $|0\rangle$ and with

core hole $|m^*\rangle$ is the eigenstate of this Hamiltonian,

$$H_s |0\rangle = (H_v + \epsilon_c) |0\rangle \equiv H_{s0} |0\rangle \tag{2.87}$$

$$H_s |n^*\rangle = (H_v + V_c) |m^*\rangle \equiv H^*_{s0} |m^*\rangle . \tag{2.88}$$

We can treat $|0\rangle$ and $|m^*\rangle$ as the direct products of core electron state and valence electron state,

$$\begin{aligned} |0\rangle &= |0_v\rangle |N_c\rangle \\ |m^*\rangle &= |N_c - 1, m\rangle |m^*_v\rangle . \end{aligned} \tag{2.89}$$

The annihilation operator b operate on the core electron state and S_n in Equation (2.42) is given as

$$\begin{aligned} S_n &= \{\langle m^*_v| \langle N_c - 1, m|\} b \{|N_c\rangle |0_v\rangle\} \\ &= \langle m^*_v| \langle N_c - 1, m| b |N_c\rangle |0_v\rangle \\ &= \langle N_c - 1, m| b |N_c\rangle \langle m^*_v|0_v\rangle \\ &\sim \langle m^*_v|0_v\rangle, \end{aligned} \tag{2.90}$$

where we ignore core electron excitations and only consider completely relaxed overlap integral $\langle N_c - 1, m| b |N_c\rangle \sim 1$. We thus obtain the intrinsic amplitudes

$$S_0 = \langle 0^*_v|0_v\rangle \tag{2.91}$$

$$S_m = \langle m^*_v|0_v\rangle \tag{2.92}$$

In order to obtain intrinsic amplitude S_m, we write $|m^*_v\rangle$ in terms of $|m_v\rangle$ by using the Hamiltonian $H_{s0} = H_v + V_c$ and conventional perturbation theory. By lowest order perturbation theory we have

$$|m^*_v\rangle = |m_v\rangle + \sum_{m'} \frac{|m'_v\rangle \langle m'_v| V_c |m_v\rangle}{E^v_m - E^v_{m'}}. \tag{2.93}$$

We can rewrite S_m as

$$\begin{aligned}\langle m_v^*|0_v\rangle &= \langle m_v|0_v\rangle + \sum_{m'} \frac{\langle m_v|\, V_c\, |m'_v\rangle}{E_m^v - E_{m'}^v}\langle m'_v|0_v\rangle \\ &= \frac{\langle m_v|\, V_c\, |0_v\rangle}{E_m^v - E_0^v}.\end{aligned} \tag{2.94}$$

The interaction between a core-hole and valence electrons V_c is given as

$$\begin{aligned}V_c &= -\sum_{ij}\langle ic|jc\rangle c_i^\dagger c_j \\ &= -\int\int \psi^\dagger(\boldsymbol{x})\phi_c^*(\boldsymbol{x}')v(\boldsymbol{r}-\boldsymbol{r}')\psi(\boldsymbol{x})\phi_c(\boldsymbol{x}')d\boldsymbol{x}d\boldsymbol{x}' \\ &= -\int\int \rho(\boldsymbol{x})v(\boldsymbol{r}-\boldsymbol{r}')|\phi_c(\boldsymbol{r}')|^2\boldsymbol{x}d\boldsymbol{x}'\end{aligned} \tag{2.95}$$

where density operator $\rho(\boldsymbol{x})$ has the relation $\rho(\boldsymbol{x}) = \psi^\dagger(\boldsymbol{x})\psi(\boldsymbol{x})$ and $\boldsymbol{x}$ denotes its coordinate $\boldsymbol{r}$ and spin. The numerator of S_m in Equation (2.94) is given as

$$\begin{aligned}\langle m_v|\, V_c\, |0_v\rangle &= \langle m_v|\left(-\int\int \rho(\boldsymbol{x})v(\boldsymbol{r}-\boldsymbol{r}')|\phi_c(\boldsymbol{r}')|^2\boldsymbol{x}d\boldsymbol{x}'\right)|0_v\rangle \\ &= -\int\int \langle m_v|\,\rho(\boldsymbol{x})\,|0_v\rangle\, v(\boldsymbol{r}-\boldsymbol{r}')|\phi_c(\boldsymbol{r}')|^2\boldsymbol{x}d\boldsymbol{x}' \\ &= -\int\int \langle m_v|\,\delta\rho(\boldsymbol{x})\,|0_v\rangle\, v(\boldsymbol{r}-\boldsymbol{r}')|\phi_c(\boldsymbol{r}')|^2\boldsymbol{x}d\boldsymbol{x}' \\ &= -\int\int v_m(\boldsymbol{x}')|\phi_c(\boldsymbol{r}')|^2 d\boldsymbol{x}' \\ &= -\langle\phi_c|\, v_m\, |\phi_c\rangle\,.\end{aligned} \tag{2.96}$$

Then we obtain the intrinsic amplitude S_m

$$S_m = -\frac{\langle\phi_c|\, v_m\, |\phi_c\rangle}{\omega_m} \tag{2.97}$$

where $\omega_m = E_m^v - E_0^v$.

Next, we will obtain intrinsic amplitude S_0 in Equation (2.91) by renormalization. Using the fact that

$$\sum_{n\neq 0}|\langle n_v^*|0_v\rangle|^2 + |\langle 0_v^*|0_v\rangle|^2 = \langle 0_v|0_v\rangle = 1 \tag{2.98}$$

we have

$$|\langle 0_v^*|0_v\rangle|^2 = 1 - a \tag{2.99}$$

with

$$a = \sum_{n\neq 0} \left| \frac{\langle \phi_c |\, v_n \,| \phi_c \rangle}{\omega_n} \right|^2 . \tag{2.100}$$

a is renormalization factor. We thus obtain the intrinsic amplitude S_0

$$S_0 = \langle 0_v^*|0_v\rangle \sim \sqrt{1-a} \sim e^{-a/2}. \tag{2.101}$$

We apply the site t-matrix expansion again to calculate the extrinsic loss term.

$$\begin{aligned} &\langle \psi_{\boldsymbol{k}}^-|v_m g(\varepsilon_p + \omega_m)\Delta|\phi_c\rangle \\ &= \langle \phi_{\boldsymbol{k}}^0|\Big(1 + \sum_{\alpha} t_\alpha g_0 + \sum_{\alpha\neq\alpha'} t_{\alpha'} g_0 t_\alpha g_0 + \cdots\Big) v_m \Big(g'_A + \sum_{\beta} g'_0 t'_\beta g'_A + \cdots\Big)\Delta|\phi_c\rangle. \end{aligned} \tag{2.102}$$

Here an abbreviation $g'_A = g_A(\varepsilon_k + \omega_m)$ is used. The damping plane wave $\phi_{\boldsymbol{k}}^0$ has complex momentum $k_z = \tilde{k}$ and real parallel components $\boldsymbol{k}_\parallel = (k_x, k_y)$,

$$\phi_{\boldsymbol{k}}^0 = \exp(i\boldsymbol{k}_\parallel \cdot \boldsymbol{r}_\parallel) \exp(i\tilde{k}z) \tag{2.103}$$

The fluctuation potential v_m defined by Equation (2.82) can be specified by wave vector $\boldsymbol{Q}_m = (q_x, q_y, 0)$ with the aid of translational symmetry parallel to the surface,

$$v_m(\boldsymbol{r}) = \exp(i\boldsymbol{Q}_m \cdot \boldsymbol{r}_\parallel) V_m(z). \tag{2.104}$$

$\boldsymbol{r}_\parallel$ is parallel component,

$$\boldsymbol{r} = (\boldsymbol{r}_\parallel, z). \tag{2.105}$$

We assume that the solid occupies the region $z \leq 0$. Then, the z component of $\phi^0_{\boldsymbol{p}}$ should be

$$\tilde{k} = \sqrt{k_z^2 - 2i\Gamma}. \tag{2.106}$$

The amplitude

$$\tau^{(0)}_{\rm ex}(\boldsymbol{k}) = \langle \phi^0_{\boldsymbol{k}} | v_m g'_A \Delta | \phi_c \rangle \tag{2.107}$$

neglects whole elastic scatterings from surrounding atoms before and after the loss. The propagator $g_A(\boldsymbol{r}, \boldsymbol{r}')$ in the amplitude $\tau^{(0)}_{\rm ex}$ is given in angular momentum representation

$$g_A(\boldsymbol{r}, \boldsymbol{r}') = -2ik' \sum_L h_l(k' r_>) Y_L(\hat{\boldsymbol{r}}) R^A_l(p' r_<) Y^*_L(\hat{\boldsymbol{r}}') \exp(i\delta^A_l), \tag{2.108}$$

where R^A_l is the regular radial solution for the spherically symmetric potential v_A at x-ray absorbing atom A. As the core function ϕ_c is strongly localized on the atomic site A, we can assumed that the condition $r > r_c \geq r'$ is always satisfied. We introduce the integral representation

$$-2ik' h_l(k' r) Y_L(\hat{\boldsymbol{r}}) = \frac{i^{-l}}{\pi^2} \int d\boldsymbol{p} Y_L(\hat{\boldsymbol{p}}) \frac{\exp(i\boldsymbol{p} \cdot \boldsymbol{r})}{k'^2 - p^2 + 2i\Gamma}, \tag{2.109}$$

and thus

$$\tau^{(0)}_{\rm ex} = \sum_L \frac{i^{-l}}{\pi^2} \int \frac{Y_l(\hat{\boldsymbol{k}})}{p'^2 - k^2 + 2i\Gamma} \langle \phi^0_{\boldsymbol{k}} | v_m | e^{i\boldsymbol{p} \cdot (\boldsymbol{r} - \boldsymbol{R}_A)} \rangle d\boldsymbol{p} M'_{LL_c}, \tag{2.110}$$

where M'_{LL_c} is an atomic excitation operator with energy $\varepsilon_k + \omega_m$.

$$M'_{LL_c}(\boldsymbol{k}) = \exp(i\delta^A_l) \rho(l)_c G(L_c 10 | L). \tag{2.111}$$

Now we evaluate the amplitude of $\langle \phi^0_{\boldsymbol{k}} | v_m | e^{i\boldsymbol{p}\cdot(\boldsymbol{r}-\boldsymbol{R}_A)} \rangle$.

$\tau^0_{\rm ex}$ is given by

$$\begin{aligned}\tau^0_{\rm ex}(\boldsymbol{k}) = \sum_L \frac{i^{-l}}{\pi^2}(2\pi)^{1/2} e^{-i\tilde{k}^* z_A} \\ \times \int dp_z \frac{Y_L(\hat{\boldsymbol{p}}')}{\kappa^2 - p_z^2 + 2i\Gamma} \int_{-\infty}^{\infty} V_m(z) e^{i(p_z - \tilde{k}^*)(z-z_A)} dz\, M'_{LL_c},\end{aligned} \tag{2.112}$$

with

$$\begin{aligned}\boldsymbol{p}' &= (\boldsymbol{k}_\parallel - \boldsymbol{Q}_m, p_z), \\ \kappa &= \sqrt{k'^2 - (\boldsymbol{k}_\parallel - \boldsymbol{Q}_m)^2} = \sqrt{k^2 + 2\omega_m - (\boldsymbol{k}_\parallel - \boldsymbol{Q}_m)^2}.\end{aligned}$$

The main contribution to the integral over p_z in Equation (2.112) comes from very small region near $p_z \sim \kappa$ because of the factor $(\kappa^2 - p_z^2 + 2i\Gamma)^{-1}$. The spherical harmonics $Y_L(\hat{\boldsymbol{p}}')$ changes very slowly with k_z and $Y_L(\hat{\boldsymbol{p}}')$ can be replaced by $Y_L(\hat{\boldsymbol{K}}')$, where

$$\boldsymbol{K}' = (\boldsymbol{p}_\parallel - \boldsymbol{Q}_m, \kappa). \tag{2.113}$$

Then the integral over p_z is calculated as

$$\int dp_z \frac{\exp[ip_z(z - z_A)]}{p_z^2 - \kappa^2 + 2i\Gamma} = \begin{cases} \frac{\pi i}{\tilde{\kappa}} e^{i\tilde{\kappa}(z-z_A)} & (z - z_A > 0) \\ \frac{\pi i}{\tilde{\kappa}} e^{-i\tilde{\kappa}(z-z_A)} & (z - z_A < 0) \end{cases}$$

$$= \frac{\pi i}{\tilde{\kappa}} e^{i\kappa|z-z_A|}, \tag{2.114}$$

with

$$\tilde{\kappa} = \sqrt{\kappa^2 + 2i\Gamma}.$$

Substituting Equation (2.114) into (2.112), Eqs. (2.115) and (2.119) are obtained.

$$\begin{aligned}\tau_{\rm ex}^{(0)}(\boldsymbol{k}) &\approx -g_{\rm ex}^{m}(A;\boldsymbol{k})\exp(-i\tilde{k}^{*}z_A)\sqrt{\frac{2}{\pi}}\sum_{L} i^{-l}Y_L(\hat{\boldsymbol{K}}')M'_{L'L_c},\\ \boldsymbol{K}' &= (\boldsymbol{k}_{\parallel}-\boldsymbol{Q}_m,\kappa),\\ \kappa &= \sqrt{k_z^2+2\omega_m-(\boldsymbol{k}_{\parallel}-\boldsymbol{Q}_m)^2}.\end{aligned} \tag{2.115}$$

The loss amplitude during the travel from site A to the detector is given by

$$\begin{aligned}g_{\rm ex}^{m}(A;\boldsymbol{k}) &= \frac{i}{\tilde{\kappa}}\Big(\int_{-\infty}^{z_A} dz\; V_m(z)e^{-i(\tilde{\kappa}+\tilde{k}^{*})(z-z_A)}+\int_{z_A}^{\infty} dz\; V_m(z)e^{i(\tilde{\kappa}-\tilde{k}^{*})(z-z_A)}\Big),\\ \tilde{\kappa} &= \sqrt{\kappa^2+2i\Gamma}.\end{aligned} \tag{2.116}$$

In the same way, an practical formula, which includes single-elastic scatterings before and after the loss, is obtained as follows:

$$\begin{aligned}\tau_{\rm ex}^{(1)}(\boldsymbol{k}) &= \sum_{\beta}\langle\phi_{\boldsymbol{k}}^{0}|v_m g_0 t_\beta g_A\Delta|\phi_c\rangle\\ &= -\sum_{\beta} g_{\rm ex}^{m}(\beta;\boldsymbol{k})e^{-i(\tilde{k}^{*}z_\beta+\boldsymbol{k}_{\parallel}\cdot\boldsymbol{R}_{\beta\parallel})}\sqrt{\frac{2}{\pi}}\sum_{LL'} i^{-l'}Y_{L'}(\hat{\boldsymbol{K}}')t_{l'}^{\beta}(k')G_{L'L}(k'\boldsymbol{R}_\beta)M'_{LL_c}\end{aligned} \tag{2.117}$$

The multiple scattering series before the loss is given by

$$\begin{aligned}&\tau_{\rm ex}^{(1)}(\boldsymbol{k})+\tau_{\rm ex}^{(1)}(\boldsymbol{k})+....\\ &\quad=\sum_{\beta} g_{\rm ex}^{m}(\beta;\boldsymbol{k})\exp\left[-i(\tilde{k}z_\beta+\boldsymbol{k}_{\parallel}\cdot\boldsymbol{R}_{\beta_{\parallel}})\right]\sqrt{\frac{2}{\pi}}\sum_{LL'\beta} i^{-l'}Y_{L'}(\hat{K}')[(1-X)^{-1}]^{\beta A}_{L'L}M_{LL_c},\end{aligned} \tag{2.118}$$

with

$$X^{\alpha\beta}_{L'L} = t_{l'}^{\alpha}(k')G_{LL'}(k'\boldsymbol{R}_{\alpha\beta})exp(-\kappa\boldsymbol{R}_{\alpha\beta})(1-\delta_{\alpha\beta}). \tag{2.79}$$

The loss amplitude $g_{\rm ex}^{m}$ defined by Equation (2.116) can be expressed in the alternative form in terms of the damping propagator g_0 written by Equation (2.65);

$$g_{\rm ex}^{m}(\beta;\boldsymbol{k}) = -(2\pi)^{3/2}\int d\boldsymbol{r}\phi_{\boldsymbol{k}}^{0*}(\boldsymbol{r})v_m(\boldsymbol{r})g_0(\boldsymbol{r}-\boldsymbol{R}_\beta;k'). \tag{2.119}$$

We have taken multiple elastic scatterings into account before the loss. We can taken then into account after the loss by replacing $\phi^{0*}_{\boldsymbol{k}}$ with $\psi^{0*}_{\boldsymbol{k}}$.

$$g^{m}_{\mathrm{ex}}(\beta;\boldsymbol{k}) = -(2\pi)^{3/2}\int d\boldsymbol{r}\psi^{0*}_{\boldsymbol{k}}(\boldsymbol{r})v_m(\boldsymbol{r})g_0(\boldsymbol{r}-\boldsymbol{R}_\beta;k'). \tag{2.120}$$

2.2 Quantum Landau Formula

Fujikawa *et al.* wrote the overall photoemission profile with elastic scattering by exponential form,

$$I(\boldsymbol{k};\omega)_c^{\infty} = |\langle\psi_{\boldsymbol{k}}^{-}|\Delta|\phi_c\rangle|^2 \times \int_{-\infty}^{\infty} dt \exp[i(\omega + E_0 - E_0^* - \varepsilon_k)t] \exp\Big[\int_0^{\infty} d\varepsilon \frac{\alpha(\varepsilon)}{\varepsilon}(e^{-i\varepsilon t} - 1)\Big], \tag{2.121}$$

where they have defined an "asymmetric function", which fully includes intrinsic and extrinsic losses. This function defined as

$$\begin{aligned} \frac{\alpha(\epsilon)}{\epsilon} &= \sum_m |\tau_m|^2 \delta(\omega - \omega_m), \\ \tau_m(\boldsymbol{k}) &= \tau_m^{\mathrm{ex}}(\boldsymbol{k}) + S_m/S_0. \end{aligned} \tag{2.122}$$

Similar quantum derivation is developed by *Hedin et al.* [8, 55] where the damping plane wave in the normal to the surface is used as the time-reversed LEED function. The damping wave function $\psi_{\boldsymbol{k}}^{-}$ is renormalized by considering the elastic scattering by neighbor atoms. Full multiple scattering formula in photoelectron diffraction can calculate the photoelectron wave amplitude $\langle\psi_{\boldsymbol{k}}^{-}|\Delta|\phi_{c_A}\rangle$ ([56, 57, 58]). The damping of the photoelectron wave should be considered from first principle theory, because the non-Hermitian optical potential affects $\psi_{\boldsymbol{k}}^{-}$. We do caliculation of the amplitude $\langle\psi_{\boldsymbol{k}}^{-}|\Delta|\phi_{c_A}\rangle$ using the quantum depth distribution function (DDF) as the function take into account the electron attenuation during its propagation [47].

Both τ_m^{ex} and S_m/S_0 can be written in terms of the fluctuation potential v_m and thus τ_m can be written as follows:

$$\tau_m(\boldsymbol{k}) = \int f_A(\boldsymbol{r}) v_m(\boldsymbol{r}) d\boldsymbol{r}, \tag{2.123}$$

$$f_A(\boldsymbol{r}) = -\frac{|\phi_c(\boldsymbol{r})|^2}{\epsilon} + (2\pi)^{3/2} \psi_{\boldsymbol{k}}^{-*}(\boldsymbol{r}) g_0(\boldsymbol{r} - \boldsymbol{R}_A; p'), \tag{2.124}$$

where $\epsilon = \omega + E_0 - E_0^* - \varepsilon_p$ is the excitation energy measured from the threshold. The first term of f_A corresonds to intrinsic losses, whereas the second one corresponds to extrinsic losses. Assuming that v_m

is always real, an alternative expression for $\alpha(\epsilon)/\epsilon$ is obtained as

$$\begin{aligned}\frac{\alpha(\epsilon)}{\epsilon} &= \int d\boldsymbol{r}d\boldsymbol{r}' f_A^*(\boldsymbol{r}')f_A(\boldsymbol{r})\sum_m v_m(\boldsymbol{r}')v_m(\boldsymbol{r})\delta(\omega-\omega_m)\\ &= -\frac{1}{\pi}\int d\boldsymbol{r}d\boldsymbol{r}' f_A^*(\boldsymbol{r}')f_A(\boldsymbol{r})\mathrm{Im}W(\boldsymbol{r},\boldsymbol{r}';\epsilon),\end{aligned} \tag{2.125}$$

where $W(\epsilon)$ is the screened Coulomb propagator. The spectral features are primarily determined by $\alpha(\epsilon)/\epsilon$.

Quantum Landau formula gives multiple plasmon loss intensity,

$$\begin{aligned}I(\boldsymbol{k};\omega)_c^\infty =&|\langle\psi_{\boldsymbol{k}}^-|\Delta|\phi_c\rangle|^2\\ &\times\exp\left[-\int_0^\infty\beta(\varepsilon')d\epsilon'\right]\left[\delta(\varepsilon)+\beta(\varepsilon)+\frac{1}{2}\beta\cdot\beta(\varepsilon)+...\right]\end{aligned} \tag{2.126}$$

where we write $\frac{\alpha(\omega)}{\omega}$ as $\beta\omega$, $\frac{\alpha(\omega)}{\omega}=\beta(\omega)$. The δ function (the first term) in Equation (2.126) gives the no loss intensity (main peak intensity), the $\beta(\varepsilon)$ (the second term) gives the single plasmon loss intensity, $\beta\cdot\beta(\varepsilon)$ (the third term) gives the double plasmon loss intensity, and so on.

2.3 Quantum One-Step Model in High Energy Approximation

In the high-energy case, the site dependence of $g^m_{\rm ex}(\beta;\boldsymbol{k})$ can be neglected [53] so $g^m_{\rm ex}(\beta;\boldsymbol{k})$ can be replaced with $g^m_{\rm ex}(A;\boldsymbol{k})$. Then in the case of high-energy region and near normal photoemission, it is possible to put $\hat{\boldsymbol{K}}' \approx \hat{\boldsymbol{k}}$. The renormalization of the multiple scattering series before the loss is written as

$$\begin{aligned}
&\tau^{(0)}_{\rm ex}(\boldsymbol{k}) + \tau^{(1)}_{\rm ex}(\boldsymbol{k}) + \cdots \\
&= -g^m_{\rm ex}(A;\boldsymbol{k}) \sum_{\beta} e^{-i(\tilde{k}^* z_\beta + \boldsymbol{k}_\parallel \cdot \boldsymbol{R}_{\beta\parallel})} \sqrt{\frac{2}{\pi}} \sum_{LL'\beta} i^{-l'} Y_{L'}(\hat{\boldsymbol{k}}) \Big[(1-X)^{-1}\Big]^{\beta A}_{L'L} M'_{LL_c} \\
&= -g^m_{\rm ex}(A;\boldsymbol{k}) \langle \psi^-_{\boldsymbol{k}'} | \Delta | \phi_c \rangle,
\end{aligned} \tag{2.127}$$

where X is defined in Eq. (2.79).

Then the full multiple scatterings are taken into account before the loss. Elastic scatterings after the loss also can be fully taken into account by replacing $\phi^{0*}_{\boldsymbol{k}}$ with $\psi^-_{\boldsymbol{k}'}$.

$$\tau_{\rm ex}(\boldsymbol{k}) \approx (2\pi)^{3/2} \langle \psi^-_{\boldsymbol{k}'} | \Delta | \phi_c \rangle \int d\boldsymbol{r} \psi^{-*}_{\boldsymbol{k}}(\boldsymbol{r}) v_m(\boldsymbol{r}) g_0(\boldsymbol{r} - \boldsymbol{R}_A; k') \tag{2.128}$$

In the high-energy photoemission, $\langle \psi^-_{\boldsymbol{k}'} | \Delta | \phi_c \rangle$ can be safely replaced with $\langle \psi^-_{\boldsymbol{k}} | \Delta | \phi_c \rangle$, which yields an approximate extrinsic loss amplitude (the second term in $|\cdots|^2$ in Eq. (2.85))

$$\begin{aligned}
&\langle \psi^-_{\boldsymbol{k}} | v_m g(\varepsilon_k + \omega_m) \Delta | \phi_c \rangle \approx \tau^{\rm ex}_m(\boldsymbol{k}) \langle \psi^-_{\boldsymbol{k}} | \Delta | \phi_c \rangle, \\
&\tau^{\rm ex}_m(\boldsymbol{k}) = (2\pi)^{3/2} \int d\boldsymbol{r} \psi^{-*}_{\boldsymbol{k}}(\boldsymbol{r}) v_m(\boldsymbol{r}) g_0(\boldsymbol{r} - \boldsymbol{R}_A; k').
\end{aligned} \tag{2.129}$$

2.4 Quantum Landau Formula for Our Studies

Here we show the formula for our numerical calculation. From quantum Landau formula in Equation (2.126), we obtain the expression for the no loss and single loss spectra,

$$I(\boldsymbol{k};\omega)^0_{c_A} = |\langle\psi^-_{\boldsymbol{k}}|\Delta|\phi_{c_A}\rangle|^2 \times \exp\left[-\int_0^\infty \beta(\varepsilon')d\epsilon'\right]\delta(\varepsilon) \tag{2.130}$$

$$I(\boldsymbol{k};\omega)^1_{c_A} = |\langle\psi^-_{\boldsymbol{k}}|\Delta|\phi_{c_A}\rangle|^2 \times \exp\left[-\int_0^\infty \beta(\varepsilon')d\epsilon'\right]\beta(\varepsilon). \tag{2.131}$$

where c_A is the core wave function at site A. Quantum Landau formula is derived within the high-energy approximation and is basically not adequate in low kinetic energy region. Ohori *et al.* have studied the applicability of this formula [59] indicating that the formula can be available also in the intermediate state (for example, several hundred eV) unless we consider grazing photoemission.

Computation of multiple-scattering costs too much because it requires a large number of matrix elements for X given in Eq. (2.79). The number of the matrix elements exponentially increases as the number of surrounding atoms or angular momentum l_{max} become larger.

For our calculations, we approximate the core function and the photoelectron wave in Eq. (2.124) as:

$$\begin{aligned} &|\phi_{c_A}(\boldsymbol{r})|^2 \approx \delta(\boldsymbol{r}-\boldsymbol{R}_A), \\ &\psi^-_{\boldsymbol{k}} \approx \phi^0_{\boldsymbol{k}}(\boldsymbol{r}) = \frac{1}{(2\pi)^{3/2}}\exp(i\boldsymbol{k}_\parallel\cdot\boldsymbol{r}_\parallel)\exp(i\tilde{k}z). \end{aligned} \tag{2.132}$$

In the approximation in Equation (2.132), we ignore elastic scatterings after the plasmon excitation and the effect of elastic scatterings for the spectral function $\alpha(\epsilon)$ are neglected for the numerical calculation. Note that we can consider elastic scattering before the excitation because the elastic scatterings are taken into account in the calculation of the amplitude $\langle\psi^-_{\boldsymbol{k}}|\Delta|\phi_c\rangle$.

We study semi-infinite jellium model so photoelectrons damp only along z-direction during their propagation inside the solid. We can treat z-axis component of momentum $\tilde{k}$ as complex number and the parallel component $\boldsymbol{k}_\parallel$ as real.

Analytical solutions for $\beta(\epsilon) = \alpha(\epsilon)/\epsilon$ are obtained by the approximations in Equation (2.132),

$$\begin{aligned}\frac{\alpha^{\mathrm{int}}(\epsilon)}{\epsilon} &= -\frac{1}{\pi}\mathrm{Im}\left[\int d\boldsymbol{r}d\boldsymbol{r}'\left(f_A^{\mathrm{int}}(\boldsymbol{r}')\right)^* f_A^{\mathrm{int}}(\boldsymbol{r})W(\boldsymbol{r},\boldsymbol{r}';\epsilon)\right] \\ &= -\frac{1}{\pi}\sum_Q \frac{1}{|\epsilon|^2}\mathrm{Im}W(Q,z_A,z_A;\epsilon) \end{aligned} \tag{2.133}$$

$$\begin{aligned}\frac{\alpha^{\mathrm{ext}}(\epsilon)}{\epsilon} &= -\frac{1}{\pi}\mathrm{Im}\left[\int d\boldsymbol{r}d\boldsymbol{r}'\left(f_A^{\mathrm{ext}}(\boldsymbol{r}')\right)^* f_A^{\mathrm{ext}}(\boldsymbol{r})W(\boldsymbol{r},\boldsymbol{r}';\epsilon)\right] \\ &= -\frac{1}{\pi}\sum_Q \frac{1}{|\tilde{\kappa}|^2}\mathrm{Im}\left[\int_{-\infty}^{\infty} dzdz' e^{i\tilde{p}(z'-z_A)}e^{-i\tilde{p}^*(z-z_A)}e^{i\tilde{\kappa}|z-z_A|}e^{-i\tilde{\kappa}^*|z'-z_A|}W(Q,z,z';\epsilon)\right] \end{aligned} \tag{2.134}$$

$$\begin{aligned}\frac{\alpha^{\mathrm{inf}}(\epsilon)}{\epsilon} &= -\frac{1}{\pi}\mathrm{Im}\left[\int_{-\infty}^{\infty} d\boldsymbol{r}d\boldsymbol{r}'\left\{\left(f_A^{\mathrm{int}}(\boldsymbol{r}')\right)^* f_A^{\mathrm{ext}}(\boldsymbol{r}) + \left(f_A^{\mathrm{ext}}(\boldsymbol{r}')\right)^* f_A^{\mathrm{int}}(\boldsymbol{r})\right\}W(\boldsymbol{r},\boldsymbol{r}';\epsilon)\right] \\ &= -\frac{1}{\pi}\sum_Q \mathrm{Im}\left[\frac{i}{\epsilon^*\tilde{\kappa}}\int_{-\infty}^{\infty} dze^{-i\tilde{p}^*(z-z_A)}e^{i\tilde{\kappa}|z-z_A|}W(Q,z,z_A;\epsilon)\right. \\ &\qquad \left. -\frac{i}{\epsilon\tilde{\kappa}^*}\int_{-\infty}^{\infty} dz' e^{i\tilde{p}(z'-z_A)}e^{-i\tilde{\kappa}^*|z'-z_A|}W(Q,z_A,z';\epsilon)\right] \end{aligned} \tag{2.135}$$

Bechstedt's screened Coulomb potential W is used to calculate $\alpha(\epsilon)/\epsilon$ [61].

$$\begin{aligned}W(Q,z,z';\epsilon) = \frac{2\pi}{Q}\Big[&\theta(z)\theta(z')\left\{e^{-Q|z-z'|} + (1-t_1)e^{-Q(z+z')}\right\} \\ &+ t_1\left\{\theta(z)\theta(-z')a(-z')e^{-Qz} + \theta(-z)\theta(z')a(-z)e^{-Qz'}\right\} \\ &+ \theta(-z)\theta(-z')\left\{a(|z-z'|) + a(-z-z') - t_1 a(-z)a(-z')\right\}\Big], \end{aligned} \tag{2.136}$$

where $a(z) = 2/\{1 + a(0)\}^{-1}$ and $a(z) \equiv a(Q,z,\omega)$ is related to the bulk dielectric function $\epsilon_0(q,\omega)$,

$$\begin{aligned}a(Q,z,\omega) = \frac{Q}{\pi}\int dq_z \frac{e^{iq_z z}}{|\boldsymbol{q}|^2\epsilon_0(|\boldsymbol{q}|,\omega)}, \\ Q = \sqrt{q_x^2 + q_y^2}. \end{aligned} \tag{2.137}$$

Chapter 3

The Plasmon Losses from Li 1s level in core-level Photoemission Spectra

3.1 Motivation of this Experiment

Typical core-level X-ray photoemission spectra have plasmon loss bands in addition to a main sharp band from simple metals and some semiconductors, notably Na, Al, Mg, Si, and Ge. The loss of energy from the photoelectron may simultaneously occur in the excitation process (intrinsic loss) or when the photoelectron travels in the solid on its way out through the surface (extrinsic loss). They can interfere each other, so these two loss mechanisms are not possible to be separated.

The quantum Landau formula originally derived by Hedin *et al*. can explain overall plasmon loss features accompanied by core level photoemission where elastic scatterings before and after the losses are completely neglected [9]. Ohori *et al*. have studied the applicability of the quantum Landau formula where they have considered no elastic scattering [59]. Their results show that the quantum Landau formula gives results quite similar to those without use of the high-energy approximation in the photoelectron kinetic energy range from 60 to 1000 eV. Uwatoko *et al*. have measured and calculated single plasmon loss spectra associated with Al 2p photoemission on the basis of Hedin's formalism [45], which shows rather good results as far as we include the interference. However, plasmon peaks are strongly influenced by the photoelectron diffraction [34], and it is thus important to consider the elastic scatterings to analyze the experimental results in detail [47].

So far Fujikawa *et al*. have derived a quantum Landau formula which fully takes multiple elastic scat-

terings before and after the losses into account [14]. This formula is a powerful tool to study the plasmon losses including higher order satellites. So far Kazama *et al*. have applied the theoretical approach to the plasmon losses associated with Al 2s and Na 2s photoemission. The single elastic scattering model gives rise to unexpected large loss intensities from deep emitters, and the overestimated strong bulk plasmon loss intensity [62].

In this work we calculate plasmon loss features associated with Li 1s photoemission using the quantum Landau formula that includes elastic multiple scatterings before and after the losses. We compare the calculated results with the plasmon losses associated with Na 2s photoemission.

3.2 Theory

We discuss only the single plasmon loss peak. From Equation (2.126), we obtain the explicit expression for single loss spectra,

$$I^1(\boldsymbol{k}) = |\langle\psi^-_{\boldsymbol{k}}|\Delta|\phi_{c_A}\rangle|^2\beta(\epsilon)\exp[-\int_0^\infty d\omega\beta(\epsilon)]. \tag{3.1}$$

3.3 Calculated result

Here we show some calculated plasmon loss profiles excited from Li 1s and Na 2s core levels by use of Equation 3.1. Figure 3.1 (a) shows the schematic view of the setup. The incident x-rays are linearly polarized and the electric vector tilts 10 degrees from the surface normal. Photon energy is 170 eV, and photoelectrons are measured normal to the surface. We use the cylinder model including 52 atoms (8 layers) which is shown in Fig. 3.1 (b).

Figures 3.2 (a) and (b) show the depth profiles of the Li 1s single loss intensity with and without full multiple-scatterings.

The ”total” shows sum of ”the intrinsic loss”, ”the extrinsic loss”, and ”the interference”. The total plasmon loss intensities without elastic scatterings in Fig. 3.2 (a) smoothly decay with increasing Z_A. Z_A is the depth of an atom which emits a photoelectron from the surface. On the other hand, in Fig. 3.2 (b), the elastic scatterings give rise to some structures caused by photoelectron diffraction from surrounding lithium atoms, although lithium atom is quite weak scatterer. The observed peaks at $Z_A = -5.23$ Å and $Z_A = -8.72$ Å correspond to the photoexcitation from the 3rd and 5th layers. These photoelectrons are

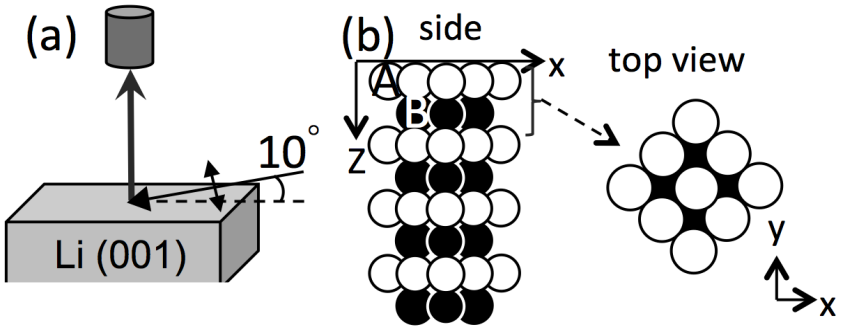

Figure 3.1: The schematic view of the calculation setup.

strongly scattered in the forward direction and provide prominent peaks. This characteristic features are noticed as ”forward focusing effect”. Lithium has a bcc structure with lattice constant 3.5 Å.

The side view shown in Fig. 3.1 (b) clearly shows that in the normal emission other lithium atoms sit on the line along surface normal for the photoemission from the 3rd and 5th layers. We thus can explain the two peaks observed in Fig. 3.2 (b). In contrast the depth profiles shown in Fig. 3.2 (a) have no such structure where no elastic scattering is taken into account there.

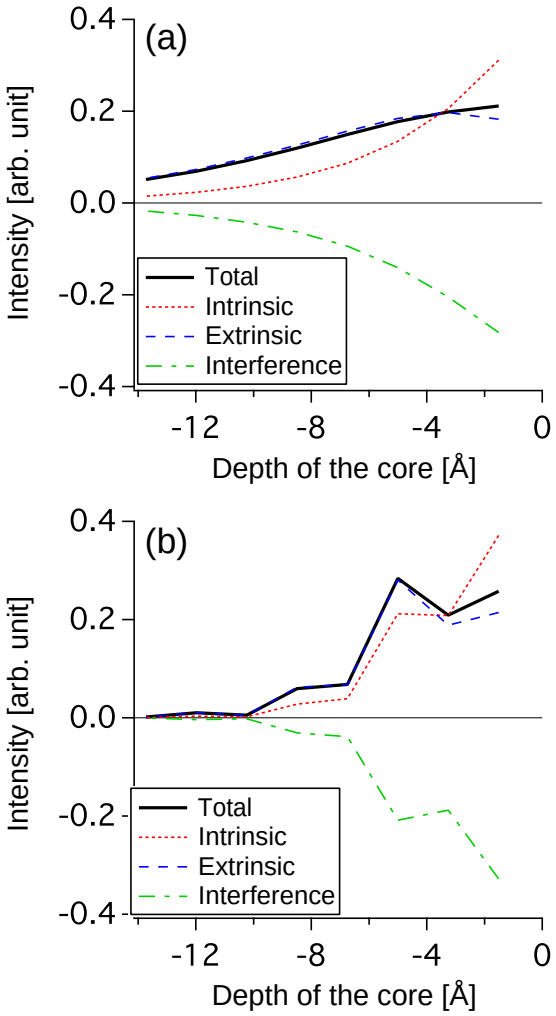

Figure 3.2: Depth profiles of integrated surface and bulk single plasmon loss intensities excited from Li 1s level. The results are shown for those calculated without elastic scatterings (a), and with full multiple-scatterings (b). The incident photon energy is 170 eV.

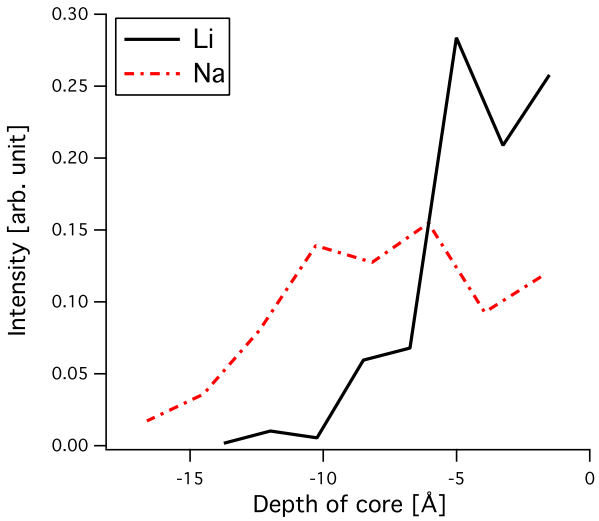

Figure 3.3: Depth profiles of integrated surface and bulk single plasmon losses excited from Li 1s and Na 2s level. The energy of photoelectrons from Li 1s and Na 2s are both about 100 eV.

Additionally the plasmon loss intensities including elastic scatterings rapidly decrease with the depth of the emitter compared with the case where elastic scatterings are neglected. This behavior can be due to defocusing effect: It has been suggested on the basis of multiple-scattering calculation that if several atoms are linearly arranged along the emission direction, the destructive interference actually reduces the intensity [35, 36]. Kazama *et al*. have investigated the Al 2s and Na 2s single-plasmon losses without elastic scatterings, with single-scatterings, and with full multiple-scatterings [62, 53]. Depth profiles of single-loss spectra of Na 2s calculated with full multiple-scatterings decay faster than without elastic scatterings. Figure 3 shows a difference between the depth profiles of the Li 1s and Na 2s single-loss intensities calculated with full multiple-scatterings. Only total intensities of plasmon losses are plotted. Sodium has the body-centered cubic structure similar to lithium metal. Therefore Na 2s photoemissions from the 3rd and 5th layer are also emphasized due to the focusing effect. The loss intensities of lithium decay faster than that of sodium because lithium is light and a weak scatterer.

Figures 3.4 (a) and (b) show the Li 1s single plasmon loss spectra calculated with and without elastic scattering. These are obtained by summing up the contributions from all of the emitters. The surface plasmon and the bulk plasmon are broad, and have clear peaks at 6 eV and 9 eV. Our calculated plasmon loss energies are larger than experimental surface and bulk plasmon energies 5.0 eV and 7.4 eV, measured by XPS [63]. In our calculation, the photoelectron kinetic energy is about 140 eV. In this low energy region, calculated energy loss peaks shift has been observed [60, 7]. Their spectral features are quite

similar although the depth profiles are quite different. In the total spectrum with full multiple-scatterings, the relative peak intensity of (surface plasmon)/(bulk plasmon) is slightly larger than that without elastic scattering. This result is against with that of sodium. It can be attributed to the faster decay as a function of the depth for Li 1s than that for Na 2s excitation.

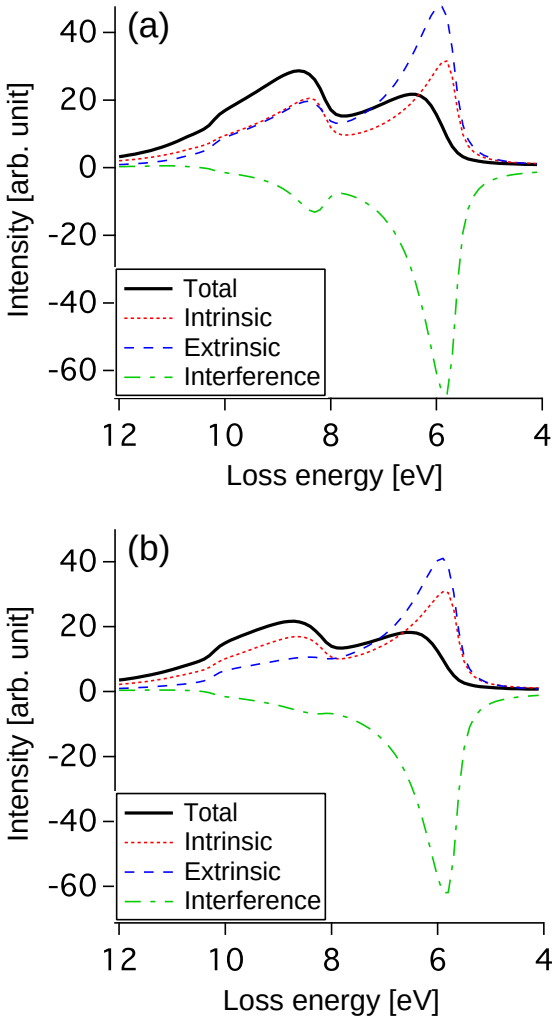

Figure 3.4: Calculated bulk and surface plasmon losses excited from Li 1s detected at normal emission with (a) and without full multiple scatterings (b).

3.4 Conclusion

In this paper we have calculated the plasmon loss features associated with Li 1s photoemission using the quantum Landau formula that includes elastic scatterings before and after the losses [14]. The quantum Landau formula allows us to calculate the multiple plasmon loss features. The depth profiles of the

Li 1s single loss intensity is considerably altered by including the elastic scatterings. When the elastic scatterings are considered, depth profiles have some peaks due to the focusing effect as observed sodium. On the other hand, these profiles of lithium decay faster than those of sodium because lithium is weak scatterer.

We also have found that the elastic scatterings can considerably change the relative intensities of bulk and surface plasmon peaks. In case of lithium, the relative peak intensity of (surface plasmon)/(bulk plasmon) is slightly larger than that without elastic scattering. This result depends on composite elements. If these elements are weak scatterers, only the shallow emitters have dominant effects on the loss spectra because of the defocusing effects.

Chapter 4

Azimuthal Angular Dependence of Plasmon Losses in Core-level Photoemission

4.1 Introduction

Plasmon produced by collective electron excitation influenced by electrical state of materials is studied in order to evaluate its mean free path and escape depth [64, 66]. Core-level X-ray photoemission spectra (XPS) have clear plasmon loss bands in low energy side in addition to the main sharp band for simple metals and semiconductors. Plasmon losses observed in XPS spectra are classified into two types: intrinsic loss (shake-up in the excitation process) and extrinsic loss (inelastic scatterings during the photoelectron propagation). We should note that these two loss can interfere each other.

Intensity of plasmon losses in photoemission bands have been studied on the point of an emission angle; polar (θ) angle and azimuthal (ϕ) angle. Biswas *et al.* studied the θ dependence of plasmon loss intensities and discussed the relative importance of intrinsic, extrinsic, and then interference [31]. Both peaks of bulk and surface plasmon have an asymmetric shape in normal emission and a symmetric shape in gazing emission. They indicated the surface the surface plasmon intensity is markedly enhanced at low θ.

Osterwalder et al. studied the ϕ scan of the plasmon losses in photoemission from Al 2s level

[34, 66]. ϕ scans of Al 2s photoelectron and plasmon loss peaks with $\theta = 45°$ are similar and show two types of peaks produced by elastic scatterings; geometrical forward-scattering peaks of [011] atoms and peaks appeared as diffraction pattern.Geometrical forward-scattering peak intensities of plasmon loss are reduced by increasing the number of plasmon loss, where photoelectrons experience energy losses as they travel from deep emitters. It follows that the defocusing effect reducing peak intensities should occur by multiple scattering effect as the emitters of photoelectrons become deeper. The defocusing effect also appeared in the multiple scattering calculation [35, 36].

In order to analyze ϕ dependance of plasmon-loss, Fujikawa's quantum Landau formula is very appropriate method because it takes multiple elastic scattering into account before and after plasmon loss [14]. The Quamtum Landau formula gives the similar results to those without the high-energy approximation in the case where the photoelectron kinetic energy is over 100 eV and the polar angle θ is over 30° [59]. By considering multiple elastic scattering, depth dependence produced by local atomic arrangements [47] and the double slit effect which occurs between two scatters can be considered[65]. Kazama *et al.* have applied these formulas to the plasmon losses excited from Al 2s and Na 2s [53]. They explain the main features observed by Biswas *et. al.*

In this work, we calculated ϕ scan of plasmon loss associated with Al 2s photoemission by using the quantum Landau formula that includes elastic multiple scatterings before and after losses. We also discuss the difference of the loss bands for the bulk plasmon and the surface plasmon loss.

4.2 Theory

We discuss only the single plasmon loss peak. From Equation (2.126), we obtain the explicit expression for single loss spectra,

$$I^1(\boldsymbol{k}) = |\langle f^-_{\boldsymbol{k}}|\Delta|\phi_{c_A}\rangle|^2\beta(\epsilon)\exp\left[-\int_0^\infty d\omega\beta(\epsilon)\right]. \tag{4.1}$$

4.3 Calculated results and discussion

Here, we show some calculated plasmon loss profiles excited from Al 2s core levels. Figure 4.1 (a) shows the schematic view of the setup.

Photon energy is 307 eV and the mean free path of photoelectron is set as 7.2 Å which is calculated

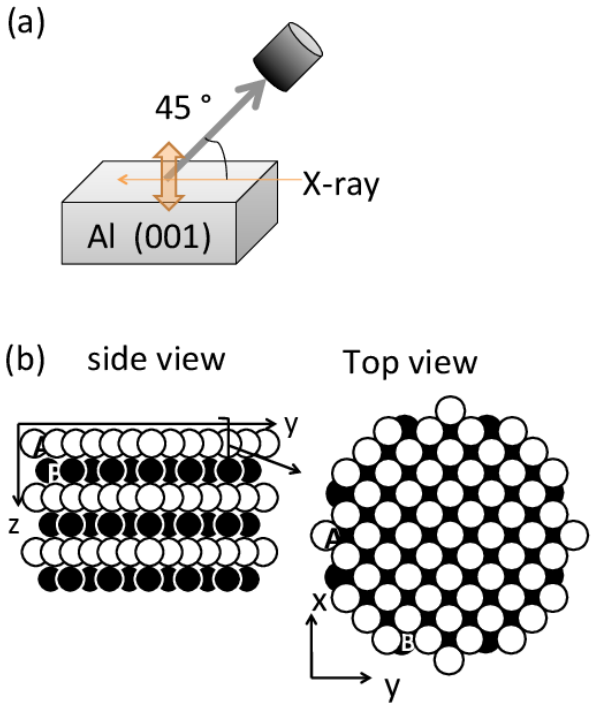

Figure 4.1: (a) The schematic view of the calculation setup. (b) The model cluster for Al (001) surface.

by TPP2M [67]. The sample and the X-ray electron vector are fixed and the position of detector is altered. The photoelectrons are detected at $\theta = 45°$ for different azimuthal angle ϕ. The azimuthal angle is set from 0° to 360° by 1° step.

The incident X-rays are linearly polarized, whose electric vector is normal to the surface. In this calculation, the effect of total reflection is not considered. This setup corresponds to the spectra of azimuthal angle scanning normalized for the polarization dependency in $\theta = 45°$. In experiment of the azimuthal scanning by Osterwalder *et al.*, the polar angle is set to 45° and the incident X-ray enters at 82° from the surface [34]. In this condition, total reflection is negligible. To make corespondent with experimental, the effect of total reflaction is not considered in the calculation. This calculation spectra is equivalent to the experimental data which is normalized by the term of the polarization dependency of linearly p wave.

We use the cylinder model including 324 atoms (six layers) shown in Fig. 4.1 (b). Aluminum has a face-centered cubic structure with a lattice constant of 4.05 Å.

A full 360° azimuthal ϕ scan of bulk plasmon loss peak for the Al 2s photoemission with full multiple scatterings is shown in Figure 4.2.

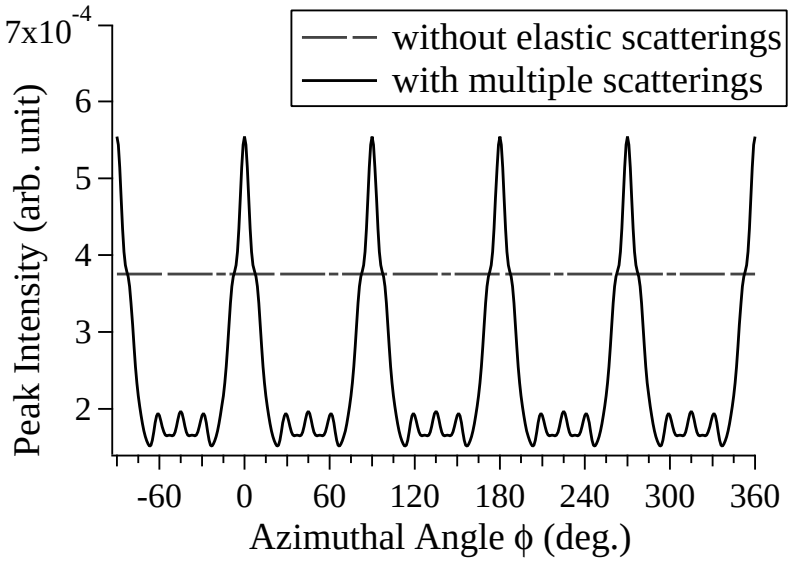

Figure 4.2: Azimuthal scans of the 1st plasmon loss in Al 2s photoemission from Al (001) single crystal calculated by quantum Landau formula (4.1) with full multiple scatterings. The incident photon energy is 307 eV.

This calculation is done by quantum Landau formula (4.1). The ϕ scan of plasmon-loss without scattering should be constant, on the other hand the ϕ scan of bulk plasmon losses with elastic scatterings shows diffraction patterns. It has similar feature with the previous experiment one [34], which clearly show the fourfold symmetry.

There are 4 prominent peaks in 360° azimuthal scan of Figure 4.2 and 3 small peaks between the prominent peaks. Prominent peaks at ϕ = 0°, 90°, 180° and 270° correspond to the forward scatterings from surrounding Al atoms along < 011 > directions. Along these directions one are linearly arranged, so that forward scatterings play an important role to these prominent peaks. This effect is called the 'forward focusing effect'. Whereas three small peaks are observed between these prominent peaks, because scattering photoelectron waves from surrounding atom interfere with each other.

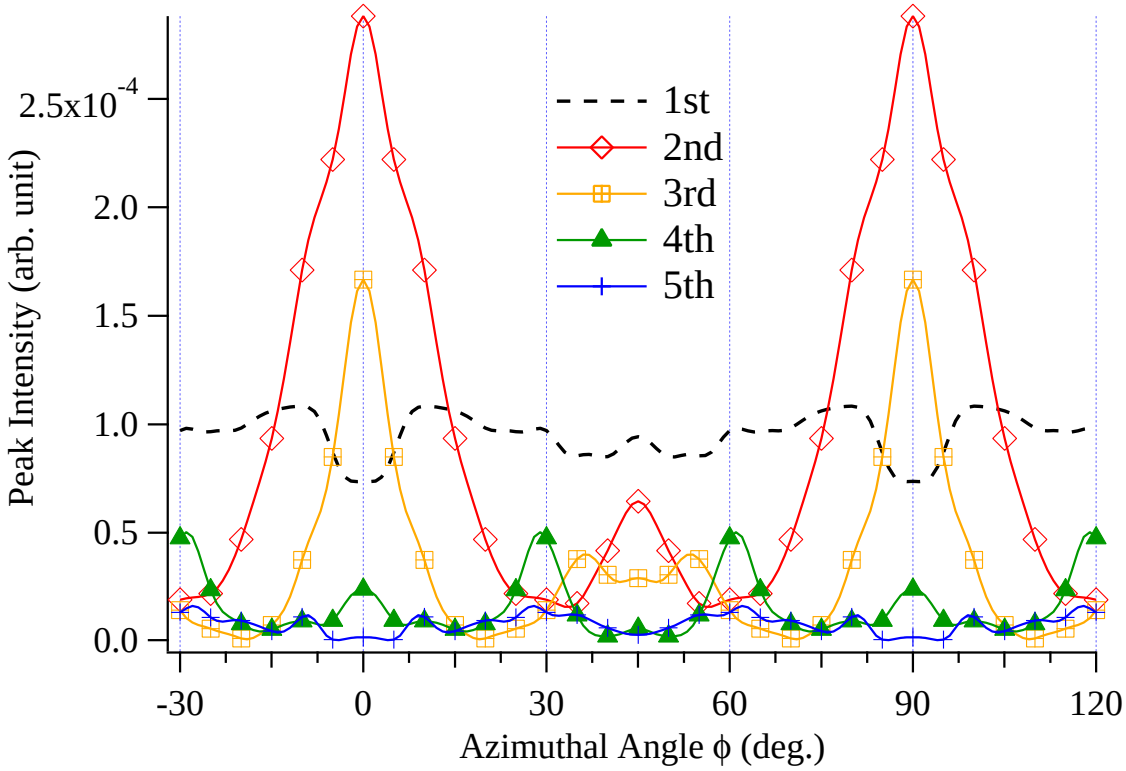

Figure 4.3: Calculated azimuthal scans of the 1st bulk plasmon loss shown in Fig. 4.2 are separately shown for each layer. Full multiple scatterings are taken into account.

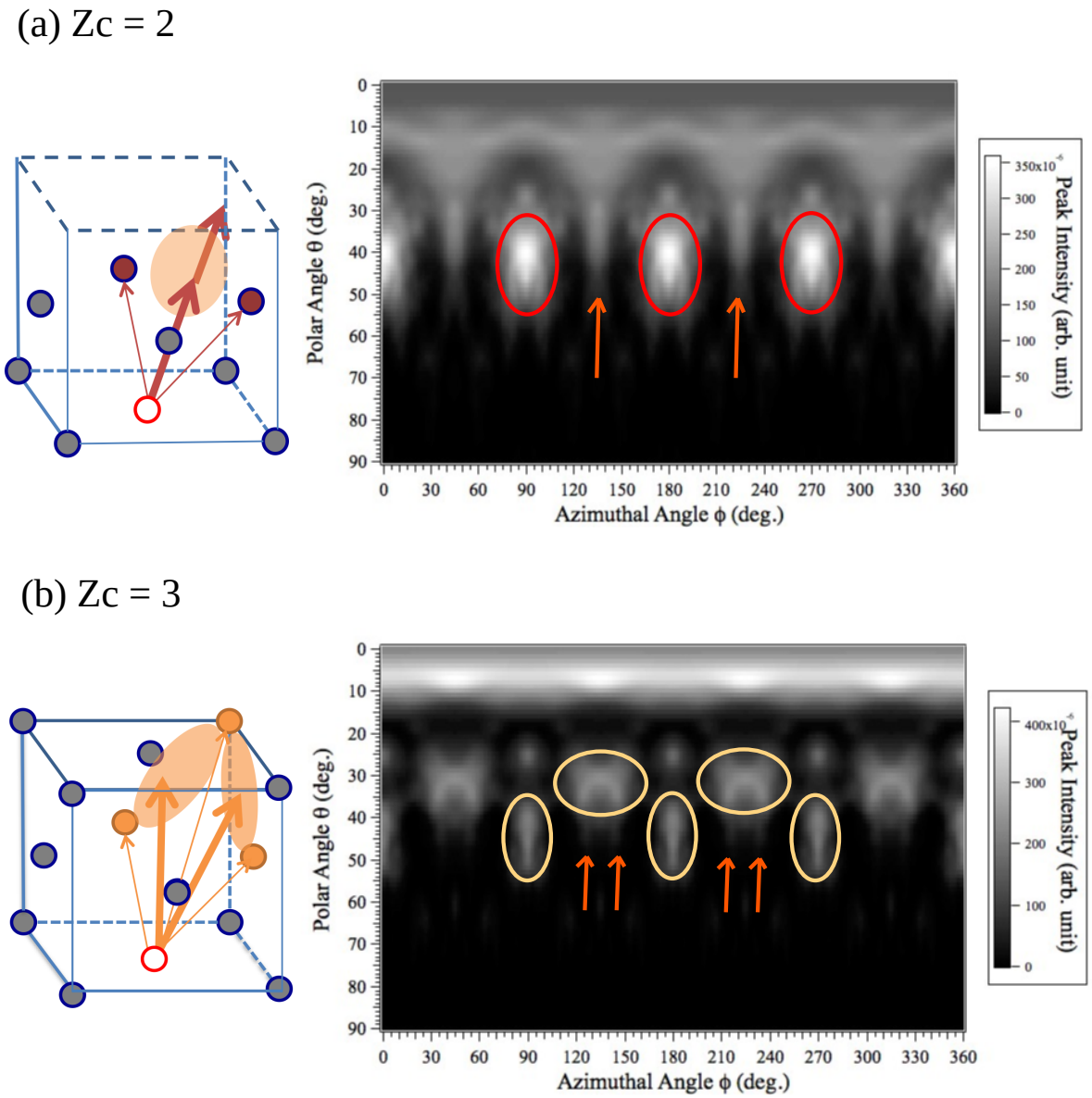

Figure 4.4: The schematic view of the model of Al single crystal and the mapping of the first plasmon loss in Al 2s photoemission spectra. (a) is explanation of the double slit peak at $\phi = 45°$ which occurs in the 2nd layer. The mapping shows the plasmon loss intensities of the 2nd layer photoelectron. (b) is the explanation of the double slit peak at $\phi = 36°$ and $54°$ in the 3rd layer. The incident photon energy is 307 eV.

Figure 4.3 shows the azimuthal scan of the 1st plasmon loss excited from each layer shown in Fig. 2. The '1st' means that the photoelectron comes from the 1st layer of model. The 1st layer means the surface layer, and the 2nd means a next layer under the 1st layer and so on. The interlayer distance is 2.03 Å.

The ϕ scan excited from the 1st layer show no prominent peak because the photoelectrons from the

1st layer never suffer forward scatterings at large take off angle. Interference of electrons scattered from different direction show the weak oscillation in the ϕ scan.

The loss band from the 2nd layer shows strong peaks at $\phi = 0°, 90°$ attributed to the forward focusing effect and a small peak at $\phi = 45°$. Small peak is attributed to the 'double slit effect' where peak intensities enhanced between two emitters. In this case, two atoms in $< 011 >$ directions in the 1st layers enhanced a peak intensity at $\phi = 45°$.

Figure 4.4 (a) shows the schematic view of the photoemission at $\theta = 45°$ and $\phi = 45°$ and the mapping of the plasmon loss emitted from the 2nd layer in Al single crystal. The schematic view shows the geometrical origin of the peaks at $\phi = 45°$ in Figure 4.3. The red lined circle is the emitter of photoelectron and the red circles are the surrounding atoms which relate the peak at $\phi = 45°$. The arrow is the direction of the photoelectron propagation. The elastic scattering waves of the red atoms in the 1st layer interfere and the peak appears by double slit effect. The circle shows the forward focusing peak by Al atom and the arrow means the double slit peak which occurred by two colored atoms at $\theta = 45°$ in the plasmon loss mapping. The peak appears between the forward focusing peak at $\phi = 0°$ and 90°.

The loss bands from the 3rd layer show two types of peak, strong peaks at $\phi = 0°, 90°$ and a small peak at $\phi = 36°$ and 54° in Figure 4.3 (a). The strong peaks are due to the forward focusing peak scattered by the atoms of the 1st layer and the 2nd layer linearly arranged in these directions. The small peak is due to the double slit effect between the 1st and 2nd layers.

Figure 4.4 (b) shows the schematic view of the photoemission at $\theta = 45°$, $\phi = 36°$ and 54°, and the mapping of the plasmon loss emitted from the 3nd layer in Al single crystal. The double slit peaks occurred between orange circles in the 1st and the 2nd layer. The direction of the atom in 2nd layer is equivalent to $\theta = 45°$ and $\phi = 0°$ and that in the 1st layer is equivalent to $\theta = 36°$ and $\phi = 45\circ$ in the angle scanning. In the plasmon loss mapping, the peaks occurs between the orange circled peak occurred the forward focusing peak of the 1st and 2nd layer atoms.

The loss band from the 4th layer shows small forward focusing peaks and relatively high peaks at $\phi = 30°$ and 60° in Figure 4.3. These peak occurred by the effect of Kikuchi electrons, which are Bragg reflected from mirror-index crystal planes and emphasized by multiple scattering waves from atoms. These peaks appears at experimental result [34]. Intensities of the loss band much smaller than the 3rd one because of the damping by the mean free path.

The forward focusing peak almost disappeared in the plasmon loss features from the 5th layer. This

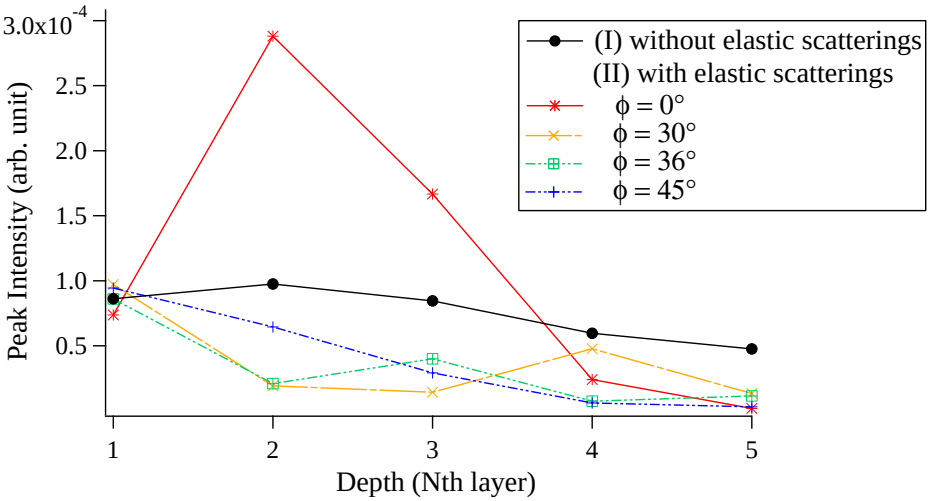

Figure 4.5: Depth profiles of the 1st bulk plasmon loss intensities excited from the Al 2s levels. The results are shown for those calculated at ϕ = 0°, 30°, 36°, 45°. The incident photon energy is 307 eV.

is because of the defocusing effect which occurs attenuation by multiple scattering in several atoms. The peaks by Kikuchi electrons can be seen at ϕ = 30° and 60° in the plasmon loss band.

Figure 4.5 shows the depth profiles of the Al 2s single loss plasmon intensities detected in ϕ = 0°, 30°, 36°,45° with and without full multiple scatterings. The total plasmon loss intensities without elastic scatterings smoothly decay with depth, which are independent on ϕ. The reason why the intensity of the 2nd layer is higher than that of the 1st one is due to the extrinsic plasmon which become higher as the emitters of photoelectrons is deeper.

Origin of peak in Figure 4.5 with ϕ = 0° in the < 011 > direction is the forward focusing effect. Peak intensity with elastic scattering does not decrease constantly. Intensities of the 2nd and 3rd layer with elastic scatterings are stronger than without elastic scatterings, on the other hand intensities of layers under the 3rd layer are lower than intensities without elastic scatterings. This is due to the ‘ focusing effect ’ and the ‘ defocusing focusing effect ’. The focusing effect, which occurs when one atom exists in forward direction of photoelectron, heightens intensities along the direction of atom. This effect appears on plasmon-loss in the 2nd layer. The defocusing effect, which occurs when several atoms exist in forward direction of photoelectron, heightens or weakens intensities. This effect appears on plasmon-loss under 3rd layer: the intensity of the 3rd layer is heightened and intensities from the 4th and the 5th layers are weaken by the defocusing effect. By the defocusing effect, the convergence is faster than that of without elastic scatterings.

In the depth profile with elastic scatterings in Figure 4.5, with $\phi = 30°$, a plasmon-loss peak at this angle appears as diffraction pattern of Kikuchi electrons. The intensities with elastic scatterings are lower than the intensities without elastic scatterings because peak intensities of this angle are reduced by interference of elastic scattering waves. The peak intensity decreases till the 3rd layer and then it rise at 4th layer and later decreases.

In the depth profile with elastic scatterings in Figure 4.5 with $\phi = 36°$, intensity decreases till the 2nd layers and peak appears at the 3rd layers and then decreases later. The large intensity at the 3rd layer is due to the double slit effect.

In the depth profile with elastic scatterings in Figure 4.5 with $\phi = 45°$, intensities at the 1st and the 2nd layers are strong and decrease under the 3rd layer. The large intensity at the 2nd layer is due to the double slit effect. Rapid decrease from the 3rd layer shows that the peaks of diffraction are easy to disappeared than the peaks by the forward focusing effect.

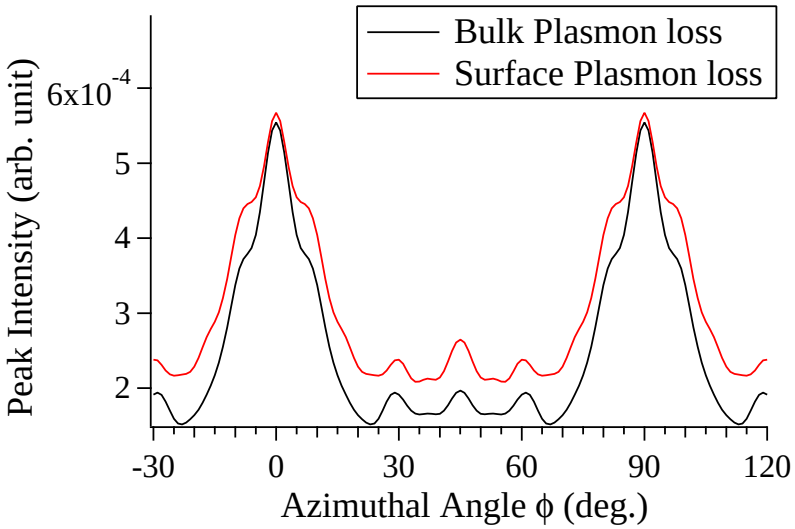

Figure 4.6: Azimuthal scans of the 1st bulk and surface plasmon loss from Al (001) surface calculated by use of full multiple scatterings.

Figure 4.6 shows the differences between ϕ scans of bulk plasmon loss and that of surface plasmon loss. In this study, bulk and surface plasmon energy is evaluated as 16.6 eV and 12.4 eV. The lowest value of peak intensities the surface plasmon is higher than that in the bulk plasmon. Comparing the feature of the bulk plasmon, the peak intensity at $\phi = 45°$ is relatively high in surface plasmon. Surface plasmon-loss intensity is dominantly attributed to photoelectrons from surface layers comparing to that of bulk plasmon. The behaviors of surface plasmon-loss have similarities with the 1st layer and the 2nd

layer.

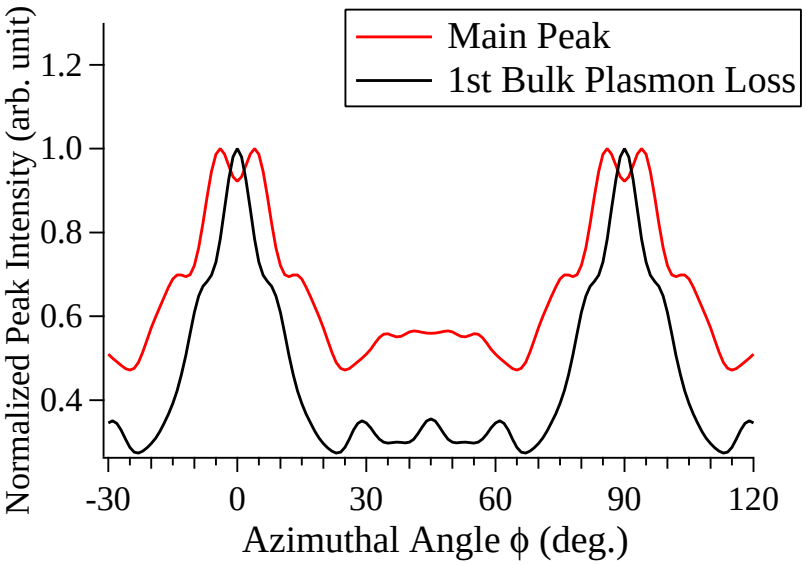

Figure 4.7: The normalized azimuthal scan of main peak and the 1st bulk plasmon loss excited from the Al 2s levels. The polar angle is set to $\theta = 45°$. The incident photon energy is 307 eV.

Figure 4.7 is shown the normalized azimuthal angle scans of the main peak and the 1st plasmon loss from Al single crystal. The lowest value of peak intensities the main peak is higher than that in the bulk plasmon. The top of forward focusing peak splits over and the peak shift of small peaks occurred. This is because the peak intensity from the surface layer is relatively high in the calculation of the main peak.

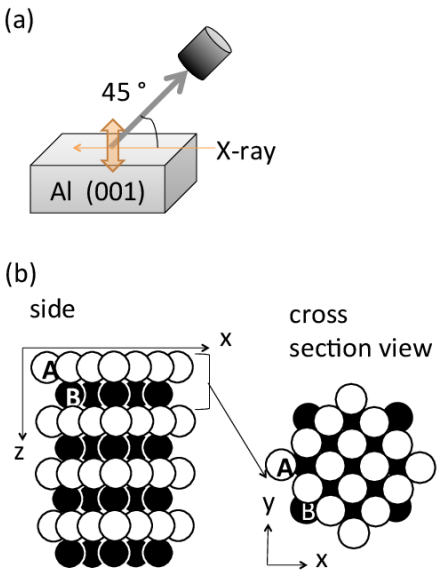

Figure 4.8: (a) The schematic view of the calculation setup. (b) The model cluster for Al (001) surface.

Figure 4.8 (a) shows the schematic view of the setup for the comparison of high and low photon energy calculation. The calculation condition is same with Figure 4.1 except the model. We use the smaller model including 116 atoms (eight layers) shown in Fig. 4.8 (b).

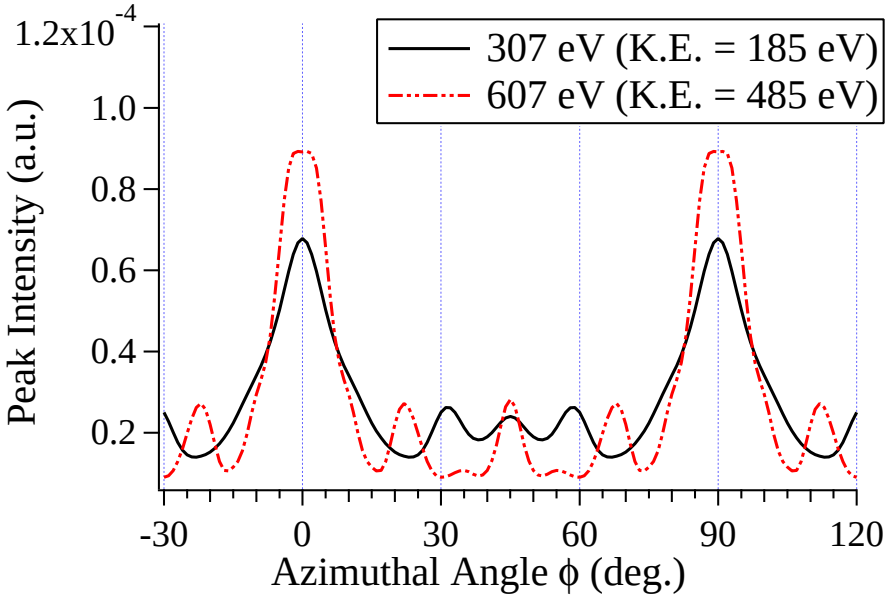

Figure 4.9: Azimuthal scans of the 1st bulk plasmon loss from Al (001) surface. The incident photon energy of solid line is 307 eV and that of dotted line is 607 eV.

Figure 4.9 shows the ϕ scans of plasmon-loss which compare the one where the photoelectron kinetic energy energy is 185 eV and the other where it is 485 eV. The plasmon-loss of 500 eV have prominent peaks at $\phi = 0°, 90°$ and small peaks at $23°, 45°, 67°$ with slight peaks appear between small peaks.These peaks are attributed to the forward focusing effect and the diffraction pattern respectively, as is the case with 185 eV. The intensities of prominent peaks are larger than that of 185 eV because more photoelectrons from deep layers are detected by increasing their mean free path. The number of peaks increase and the peak widths are narrower than that of 185 eV. This is because diffraction pattern become more complicated by increasing photoelectron kinetic energy.

4.4 Conclusion

In this paper, we have calculated the azimuthal scan of the plasmon loss associated with Al 2s photoemission using the quantum Landau formula that includes elastic scatterings before and after losses. The azimuthal scans with elastic scattering well replicated the previous experimental one whereas these

without elastic scatterings could not. The azimuthal scans separated by layers clearly show the influence of the 'forward focusing effect' and 'double slit effect'. The depth profiles of peak intensities on the direction of $< 011 >$ have peaks as a result of the focusing effect and the intensities decreases by the defocusing effect as the emitter exists deeper. The double slit peak appeared between atoms near the emitters. The differences of structure in azimuthal scans can be seen in bulk and surface plasmon peaks. This is because surface plasmon occurs near surface. The forward-scattering peaks became strong as the photoelectron kinetic energy energy became high due to the increase of the photoelectron from deep layers.

Chapter 5

Conclusion

We have theoretically studied the energy dependence of surface and bulk plasmon losses in Li 1s photoemission spectra and the azimuthal angular dependence of surface and bulk plasmon losses in Al 2s photoemission spectra. Here, full multiple scatterings of photoelectrons are taken into account before and after plasmon losses within the quantum Landau formula, which can describe overall features of the photoemission bands. We discussed depth profile and energy dependence in the calculation of one plasmon loss of Li solid. Comparing the depth dependence with elastic and inelastic scattering, we found that the intensity of plasmon loss with elastic scattering is affected by defocusing effect, it follows that the intensity become lower than that without elastic scattering. Li is light element, but it reflects the effect of elastic scattering clearly. Comparing Li and Na, the intensity of photoelectron in Li is lower and decay faster than that in Na.

We also discussed depth profile and azimuthal dependence in the calculation of single plasmon loss in Al XPD. When the elastic scattering is not taken into account, the intensity of single plasmon loss doesn't depend on azimuthal angles. In the calculation of plasmon loss with full multiple scattering, we acquired the similar result as the XPD plasmon loss patterns in the experiment [34]. The XPD patterns for the single plasmon loss depend on the geometrical structure; there observed forward focusing peaks and double slit peaks in XPD patterns for plasmon loss.

The quantum landau Formula contains the elastic scattering effect. We can calculate the intensity of photoelectrons introducing the effect, and we found that contribution of photoelectron emission from the shallow layers for the total emission in the calculation with elastic scattering is larger than that without it.

Acknowledge

I would like to express my heartfelt gratitude to Prof. Takashi Fujikawa for his continuing guidance, help, and encouragement. I would like to express my appreciation to Prof. Takehisa Konishi. Insightful comments and suggestions by Prof. Konishi have improved my study and method of thinking. I am deeply grateful to Dr. Kaori Niki for her discussion and kindly encouragement. I deeply thank Prof. Laszlo Kover for his guidance, advice and recommendations for my plasmon studies. I deeply thank Prof. Nobuyuki Aoki, Prof. Peter Krüger, and Prof. Kazuyuki Sakamoto for guidances, advices and recommendations throughout the review of this thesis. I am truly thankful to Dr. Hiroshi Shinotsuka (Advanced Algorithm and Systems Co., Ltd.), who was formerly a member of Fujikawa group in Chiba University, for his generous assistance and advices for our programming source code. I deeply thank Mr. Ohori Yusuke (Ibaraki University), who was formerly a member of Fujikawa group in Chiba University, for her generous assistance and helpful comments for plasmon studies. I would like to express my gratitude to Dr. Kazama Misato (Ashahi Kasei Co., Ltd.), who was formerly a member of Fujikawa group in Chiba University, for her generous assistance and helpful comments for plasmon studies. I thank Mr. Nobuyuki Tamura for his kindness and discussions. I thank all members of Konishi-Niki group for their kindness and assistance. My study life has been delightful thanks to the great friends. Finally I would like to express my deep gratitude to my parents, Hitoshi and Yuki for their understanding, support, and encouragement throughout my study.

References

[1] A. D. Baker and C. R. Brundle, in *An Introduction to Electron Spectroscpy*, edited by C. R. Brundle and A. D. Baker, Academic Press; London ; New York, vol. 5, p.307 (1977).

[2] H. Hertz, *Ann. Physik*, 31, 983 (1887).

[3] A. Einstein, *Ann. Physik*, 17, 132 (1905).

[4] K. Seigbahn, C. Nordling, A. Fahlman, R. Nordberg, K. Hamrin, J. Hedman, G. Johansseon, T. Bergmark, S. Karlsson, I. Lindgren, and B. Lindberg, *ESCA-Atomic, Molecular and Solid State Structure Studied by means of Elecron Spectroscopy* Uppsala : Almqvist and Wickcells, 1967).

[5] L. Hedin and S. Lundqvist, *Effects of Electron-Electron and Electron-Phonon Interaction on the One-Electron States of Solids* In *Solid State Physics*, Ed. S. Frederic, D. Turnbull, and H. Ehrenreich, **23**, p.1 - 68 (1969).

[6] C.-O. Almbladh and L. Hedin "Beyond the One-Electron Model. Many-Body Effects in Atoms, Molecules, and Solids" *Handbook on Synchrotron Radiation 1b.* Ed. E. E. Koch, Amsterdam: North-Holland p.607-904, (1983).

[7] W. Bardyszewski and L. Hedin, *Phys. Scr.* **32**, 439 (1985).

[8] L. Hedin, in *Recent Progress in Many-Body Theories*, edited by A. J. Kallio, E. Pjanne, and R. F. Bishop, Plenum; New York, vol. 1, p.307 (1988).

[9] L. Hedin, J. Michiels, and J. Inglesfield, *Phys. Rev. B*, **58**, 23, 15565, (1998).

[10] T. Fujikawa and H. Hedin, *Physical Review B*, **40**, 17, 11507 (1989).

[11] T. Fujikawa and L. Hedin, *Phys. Rev. B*, **40**, 17, 11507, (1989).

[12] T. Fujikawa,“ Electron Energy Loss Spectroscopy for Surface Study. ”*Handbook of Thin Film Materials, Volume2: Characterization and Spectroscopy of Thin Films.* Ed. H. S. Nalwa. By Academic Press, 415, (2002).

[13] T. Fujikawa and H. Arai, *J. Elect. Spect. Related Phenom.*, **123**, 1, 19 (2002).

[14] T. Fujikawa, M. Kazama, H. Shinotsuka, *e-J. Surf. Sci. Nanotech.*, **6**, 263 (2008).

[15] ”dielectric function 誘電関数”, *Rikagaku Dictionary* 理化学事典, Ed. S. Nagakura, H. Iguchi, H. Ezawa, H. Iwamura, H. Satou, and R. Kubo, 5th ed. (1998).

[16] C. Kittel, *Introduction to Solid State Physics* (8th ed.) (Trans. R. Uno, N. Tsuya, K. Niizeki, A, Morita, and J. Yamashita). New York: John Willey, (2005).

[17] D. Y. Smith, E. Shilies and M. Inokuti,“ The Optical Properties of Metallic Aluminum ”In E. D. Palik, *Handbook of Optical Constants of Solids* (Vol. 1)., (p.369 - 406) Amsterdam: Elsevier, (1985).

[18] E. Shilie, T. Sasaki, M. Inokuti, and D. Y. Sumith, *Phys. Rev. B*, **22**, 1612 (1980).

[19] G. Quincke, *Ann. Physik, Series 2, Jubelband*, p. 336 (1874).

[20] W. Voigt, *Ann Physik, Series 3*, **23**, 142 (1884).

[21] F. F. Martens,“ Landolt-Börmstein ”Vol.2 5th ed., Section 165, p. 906. Berlin: Springer, (1923).

[22] A. G. Mathewson and H. P. Myers, *Phys. Scr.* **4**, 291 (1971).

[23] H. Raether, *Excitation of Plasmons and Interband Transitions by Electrons*, Springer Tracts in Modern Physics, vol. 88, S Berlin : pringer-Verlag, (1997).

[24]“ plasmon プラズモン ”, *Rikagaku Dictionary* 理化学事典, Ed. S. Nagakura, H. Iguchi, H. Ezawa, H. Iwamura, H. Satou, and R. Kubo, 5th ed. (1998).

[25] L. Lindau and P. O. Nilsson, *Phisics Letters*, **31A**, 7, 352 (1970).

[26] G. Ruthemann, *Naturwissenschaften*, **30**, 145 (1942).

[27] G. Ruthemann, *Ann. Phys.*, **2**, 133 (1948).

[28] C. J. Powell and J. B. Swan *Physical Review*, **115**, 4, 896 (1959).

[29] K. A. Mkhoyan, T. Bainec, S. E. Maccagnano, E. J. Kirkland and J. Silcox *Ultramicroscopy*, **107**, 345 (2007).

[30] S. Hufner, *Photoelectron Spectroscopy, Springer Series in Solid-State Sciences*, vol. 82, Berlin : Springer, (1995).

[31] C. Biswas, A. K. Shukla, S. Banik, V. K. Ahire and S. B. Barman *Phys. Rev. B*, **67**, 165416 (2003).

[32] C. S. Fadley *Nuclear Indtruments and Methods in Physics Research A*, **547**, 24, (2005).

[33] C. S. Fadley *Chapter in Synchrotoron Radiation Research: Advances in Surface and Interface Science* Ed. R. Z. Bachrach, New York; Plenum Press (1992).

[34] J. Osterwalder, T. Greber, and S. Hüfner, L. Schlapbash, *Phys. Rev. B* **41**, 18, 12495 (1990).

[35] Y. Tong, H. C. Poon, and D. R. Snider, *Phys, Rev. B* **32**, 2096 (1985).

[36] M. L. Xu, J. J. Barton, and M. A. Van Hove, *Phys. Rev. B* **39**, 8275 (1989).

[37] C. N. Bergulund and W. E. Spicer *Physical Review*, **136**, A1030 (1964).

[38] A. C. Simonen, Y. Yubero, and S. Tougaard, *Phys. Rev. B* **71**, 045414 (2005).

[39] S. Tougaard *Surf. Sci.*, **464**, 233 (2000).

[40] Y. Yubero and S. Tougaard, *Phys. Rev. B*, **71**, 045414 (2005).

[41] W. S. M. Werner, L. Köver, S. Egri, J. Tóth, and D. Varga, *Surf. Sci.* **585**, 85 (2005).

[42] J. E. Inglesfield, J. Phys. C: *Solid State Phys.* **16**, 403, (1983).

[43] S. A. Flodström, R. Z. Bachrach, R. S. Bauer, J. C. McMenamin and S. B. M. Hagström, *J. Vac. Sci. Technol.* **14**, 303 (1977).

[44] L. I. Johansson and I. Lindau, *Solid State Commun.*, **29**, 379 (1979).

[45] T. Uwatoko, H. Tanaka, K. Nakayama, S. Nagamatsu, K. Hatada, T. Konishi, T. Fujikawa, T. Kinoshita, A. Harasawa, and A. Kakizaki, *J. Surf. Sci. Jpn.*, **22**, 497, (2001).

[46] X. Ashley and R. H. Ritchie, *Phys. Rev.* **174**, 1572 (1968).

[47] H. Shinotsuka, H. Arai, and T. Fujikawa, *Phys. Rev. B* **77**, 085404, (2008).

[48] T. Fujikawa, *J. of the Phys. Society of Japan*, **60**, 11, 3904 (1991).

[49] M. L. Goldberger and K. M. Watson, *Collision Theory* NewYork : Wiley (1964).

[50] B. I. Lundqvust, *Phys. Kondens. Mater.*, **9**, 236 (1969).

[51] D. C. Langreth, *Phys. Rev. Lett.*, **26**, 1229 (1971).

[52] J. E. Inglesfield, *Sol. St. Comm.* **40**, 467, (1981) .

[53] M. Kazama, H. Shinotsuka, Y. Ohori, K. Niki, T. Fujikawa and L. Kövér, *Phys. Rev. B*, **89**, 045110, (2014).

[54] L. Van Hove, *Physica* , **21** 901 (1955).

[55] L. Hedin "3. General theory of core electron photoemission", *Solid-State Photoemission and Related Methods* Ed. W. Schattke and M. A. Van Hove, Wiley-VCH; New York p.116-140 (2003).

[56] T. Teramoto, J. Adachi, M. Yamazaki, K. Yamanouchi, M. Stener, P. Decleva, A. Yagishita, *J. Phys. B*, **40**, 4033 (2007).

[57] A. M. Kondratenko and E. L. Saldin, *Part. Accel.* **10** 207 (1980).

[58] A. H. Zewail, *J. Phys. Chem. A*, bf 104, 5660 (2000).

[59] Y. Ohori, H. Shinotsuka, M. Kazama, and T. Fujikawa, e-J. Surf. Sci. Nanotech., **10**, 145, (2012).

[60] T. Fujikawa *J. Phys. Soc. Jpn. Scr.* **32**, 439, (1985).

[61] F. Bechsted, R. Enderlein and D. Reichardt, *Phys. Status Solid b*, **117**, 261 (1983).

[62] M. Kazama, H. Shinotsuka, Y. Ohori and T. Fujikawa, *e-J. Surf. Sci. Nanotech.*, **10**, 331 (2012).

[63] S. P. Kowalczyk, L. Ley, F. R. McFeely, R. A. Pollak and D. A. Shirley, *Phys. Rev. B* 8, 3583, (1973).

[64] T. Miyanaga, M. Nakamae, H. Nago, Y. Ohori and T. Fujikawa, *e-J. Surf. Sci. Nanotech.*, **10**, 565 (2012).

[65] M. Kazama, H. Shinotsuka, M. Yamazaki, J. Adachi, A. Yagishita, and T. Fujikawa, *J. Phys. Conf. Series* **190**, 012048 (2009).

[66] S. Hüfner, J. Osterwalder, T. Greber, and L. Schlapbach, *Phys. Rev. B*, **42**, 12, 7350 (1990).

[67] S. Tanuma, C. J. Powell, D. R. Penn, *Surf. Interf. Anal.* **21**, 165 (1994).